NASA CR-147454

EPN 108   E7.6-10.19.3

P.I. DR. GEORGE MAUL

105036

NASA CR- 147454

EPN 108 E 7.6 - 1 0.1 9.3

P.I. DR. GEORGE MAUL

An Experiment to Evaluate SKYLAB Earth Resources
Sensors for Detection of the Gulf Stream

A FINAL REPORT TO NASA

By George A. Maul
Howard R. Gordon *
Stephen R. Baig **
Michael McCaslin
Roger J. DeVivo

National Oceanic and Atmospheric Administration
Atlantic Oceanographic and Meteorological Laboratories
15 Rickenbacker Causeway
Miami, Florida 33149

University of Miami *
Coral Gables, Florida

Nova University **
Dania, Florida

T-4713B

1976

CONTENTS

AN EXPERIMENT TO EVALUATE SKYLAB EARTH RESOURCES
SENSORS FOR DETECTION OF THE GULF STREAM

George A. Maul
Howard R. Gordon
Stephen R. Baig
Michael McCaslin
Roger J. DeVivo

An experiment to evaluate the SKYLAB Earth Resources Package for observing ocean currents was performed in the Straits of Florida in January 1974. Data from the S-190 photographic facility, S-191 spectroradiometer, and the S-192 multispectral scanner, were compared with surface observations made simultaneously by the R/V VIRGINIA KEY and the NASA C-130 aircraft. The anticyclonic edge of the Gulf Stream could be identified in the SKYLAB S-190 A and B photographs, but the cyclonic edge was obscured by clouds. The aircraft photographs were judged not useful for spectral analysis because vignetting caused the blue/green ratios to be dependent on the position in the photograph. The spectral measurement technique could not identify the anticyclonic front, but a mass of Florida Bay water which was in the process of flowing into the Straits could be identified and classified. No calibration was available for the S-191 infrared detector, so the goal of comparing the measurements with theoretical calculations was not accomplished. Monte Carlo simulations of the visible spectrum showed that the aerosol concentration could be estimated and a correction technique was devised. The S-192 scanner was not useful for detecting the anticyclonic front because the radiance resolution was inadequate. An objective cloud discrimination technique was developed; the results were applied to the several useful oceanographic channels to specify the radiance ranges required for an ocean tuned visible multispectral scanner.

1. INTRODUCTION

An important problem in physical oceanography is the location of the boundaries of surface currents. Many techniques have been proposed to study such boundaries from space, but the actual process of extracting the correct information from satellite data is in the early stages of development. SKYLAB, with its several types of sensors (NASA, 1975), afforded the opportunity to test three techniques simultaneously: photography, spectroscopy, and multispectral imagery.

1.1 Background and Purpose

Major ocean currents are known to have several observable surface features that make them distinguishable from the surrounding waters. The Gulf Stream system is used as an example to typify these changes because it is one of the most important ocean currents, and because understanding its features permits one to study other current systems.

Because of its subtropical origin, the current is typically warmer than surrounding waters and thus has a surface thermal signature that often can be detected in infrared imagery. The waters of the current are also much lower in biological productivity and hence there are fewer particles and biological pigment molecules in the Stream; this translates to water of a deep blue color. Conversely, the juxtaposed water masses are frequently higher in biological productivity, and this can cause that water to be greener. Another feature of the current that makes it visibly distinguishable is caused by the large horizontal velocity shear. Frequently the faster moving water in the current has a different sea state than surrounding waters. Just as common are the many slick lines associated with the shear. Finally, the atmosphere above the Gulf Stream is modified under certain conditions which can also give an indication of the current's location.

There are several other features of the Gulf Stream that are potentially detectable by satellite altimetry and other microwave techniques. The measurement of these parameters will not be discussed in this report, the approach here being confined to visible and infrared wavelengths. The final goal of this experiment is to contribute to the multi-parameter determination of the location of the Gulf Stream, of which visible and infrared measurements of radiance are an integral part.

1.2 Test Site

The experiment was conducted in the Straits of Florida along a sub-orbital track in the vicinity of Key West, Florida. In this channel, the Gulf Stream runs approximately perpendicular to the satellite ground track. This would maximize the change in oceanic variables while minimizing the impact on the data acquisition facility onboard SKYLAB. Furthermore, the logistics of performing the sea truth from a 65 foot vessel in January weather made the choice of a semi-protected body of water mandatory.

Hydrographic conditions in the test site are controlled by the location and intensity of the Gulf Stream (also called the Florida Current in this vicinity). The cyclonic edge, defined as the left hand edge facing downstream, has horizontal excursions of approximately 50 km; that is, at some times of the year the current's edge may be found 20 km. south of Key West and at other times 70 km to the south (Maul, 1975). The location of the cyclonic front determines the location of the major hydrographic features of the Straits. Materials from Florida Bay are also known to flow into the straits and at times become entrained in the current. The detection of occurences involving mixing of Gulf Stream and Florida Bay waters is of fundamental importance to the dispersal of natural and man-introduced materials.

1.3 Prior Investigations

A general review of remote sensing of ocean color was given by Hanson (1972), and Maul (1975) discussed the application of visible spectroscopy to locating ocean current boundaries. Gordon, in a series of papers (e.g. Gordon, 1973; Gordon and Brown, 1973; Maul and Gordon, 1975) discussed the

spectra of upwelling irradiance as a function of the optical properties of the water as calculated by Monte Carlo simulations; those studies are directly related to the current boundary location problem because the spectrum of light changes from Gulf Stream water to coastal water. Techniques for determining ocean chlorophyll (e.g. Baig and Yentsch, 1969; Mueller, 1973; Duntley et al., 1974) are also related to current boundary determination because pigment forming molecules, along with suspended materials, affect the light spectrum.

Remote sensing of ocean currents in the infrared region of the electromagnetic spectrum has been attempted for many years (e.g.: Warnecke, et al., 1971; Hanson, 1972; Richardson, et al., 1973). However, there have been questions concerning the radiative transfer model dependency of the atmospheric correction (Maul and Sidran, 1972; Anding and Kauth, 1972) that have awaited SKYLAB to be addressed. Adequate atmospheric correction techniques are required for ocean current boundary determination using once or twice daily observations because compositing of images is required in order to fill in the areas covered by clouds; composites must be based on a common measurement, that of the sea surface temperature itself.

SKYLAB provided the first opportunity to evaluate photographic, spectrometric, and multispectral imagery in a specific experiment designed for current boundary location. It will be seen that each instrument has unique advantages, disadvantages, and limitations. It is the intent of this report to objectively evaluate each technique and provide recommendations for future equipment and measurements.

2. GROUND TRUTH DATA

This section gives the details of how the ocean surface data were obtained, calibrated, and analyzed. In many cases the surface optical measurements are useful indicators of the properties of the water that need to be measured. This is because the theory is well ahead of the measurements and adequate instruments are not yet designed or built. In the case of spectrometer measurements, the ideal observations are in fact physically impossible.

2.1 Cruise Report

The at-sea observations were designed to provide simultaneous measurements of the ocean while the aircraft and satellite transited the area. Since the speeds of the three vehicles are mismatched, the assumption must be made that the oceanic conditions are a steady-state for 12 hours or so. While it is recognized that this is not strictly true, it is necessary in view of resources available.

Weather conditions for the experiment were not ideal, with partly cloudy skys and moderate seas. Wind was from 045° at 4ms^{-1} and remained steady most of the day. Air temperature ranged from 23.8°-26.1°C, wet bulb values were 23.0°C most of the day. Visibility was 20 km except in a rain shower at 1700 GMT where it dropped to less than 5 km. Barometer was steady at 1025 mb until 1900 GMT when it abruptly dropped to 1023 mb and remained so thereafter. Wave height was 1/4 meter until 2100 GMT when it abruptly

increased to 1/2 meter; period remained 4 seconds throughout the day.

Underway operations on the Virginia Key included gathering data on ocean salinity, chlorophyll-a concentration, surface nutrients, seawater scattering properties, sea surface temperature by bucket and by a continuous radiometric profile, and ocean temperature down to 450 m with expendable bathythermographs; ship was hove-to for spectrometry observations. Collection of this data started at 24° 39'.1 N, 81° 08'.1 W at 1253 GMT, 8 January 1974. This point is about 7 km . SSE of Marathon in the Florida Keys. The track was directed SW and ended at 23° 33'.2 N, 81° 55'.5 W at 0150 GMT 9 January. This is 41 km . off the north coast of Cuba on the evening of the same day.

The Virginia Key travelled at a speed of 8 knots while on track. The boat stopped only for spectrometry stations; all the trackline profile data was collected while making speed.

2.2 Trackline Profile Data

Figure 2.1 is a plot of the trackline data, after reduction. The stipled profile below the 22°C isotherm shows the bottom profile along the track. The arrow shows where the 22°C isotherm crosses a depth of 100 m, a point interpreted to be approximately 15 km south of the boundary of the Gulf Stream (Maul, 1975). The $\beta(45)$ curves show the volume scattering function at 45 degrees, and are in units of meter^{-1} steradian^{-1} (m^{-1} sr^{-1}).

A detailed discussion of the data collection, reduction, and interpretation follows.

a) Chlorophyll-a (Cl-a)

Cl-a concentrations were obtained continuously by measuring the fluorescence of Cl-a when exposed to blue light. The data are reported as if all the pigment forming molecules (including pheophytins) were chlorophylls. The continuous record was obtained using a Turner fluorometer, Model 111, which measured the fluorescence of surface water drawn thru a continuous-flow intake system. This method is as described in Strickland and Parsons (1968), with the addition of a bubble trap. In order to calibrate the continuous record, three discrete samples were obtained by filtration and measured against a known standard after the cruise. This also was as described by Strickland and Parsons (1968) , and uses the SCOR/UNESCO equation. Table A.1 in Appendix A shows the times and positions of the three samples.

The large gap in the Cl-a curve on Fig. 2.1 is due to a combination of drift on a particularly long spectrometry station and a delay in turning on the fluorometer after leaving the station. The three other breaks in the record represent a change in fluorescence while stopped for short spectrometry stations. The degree of variability in Cl-a concentration over the short distances indicated in the record shows the
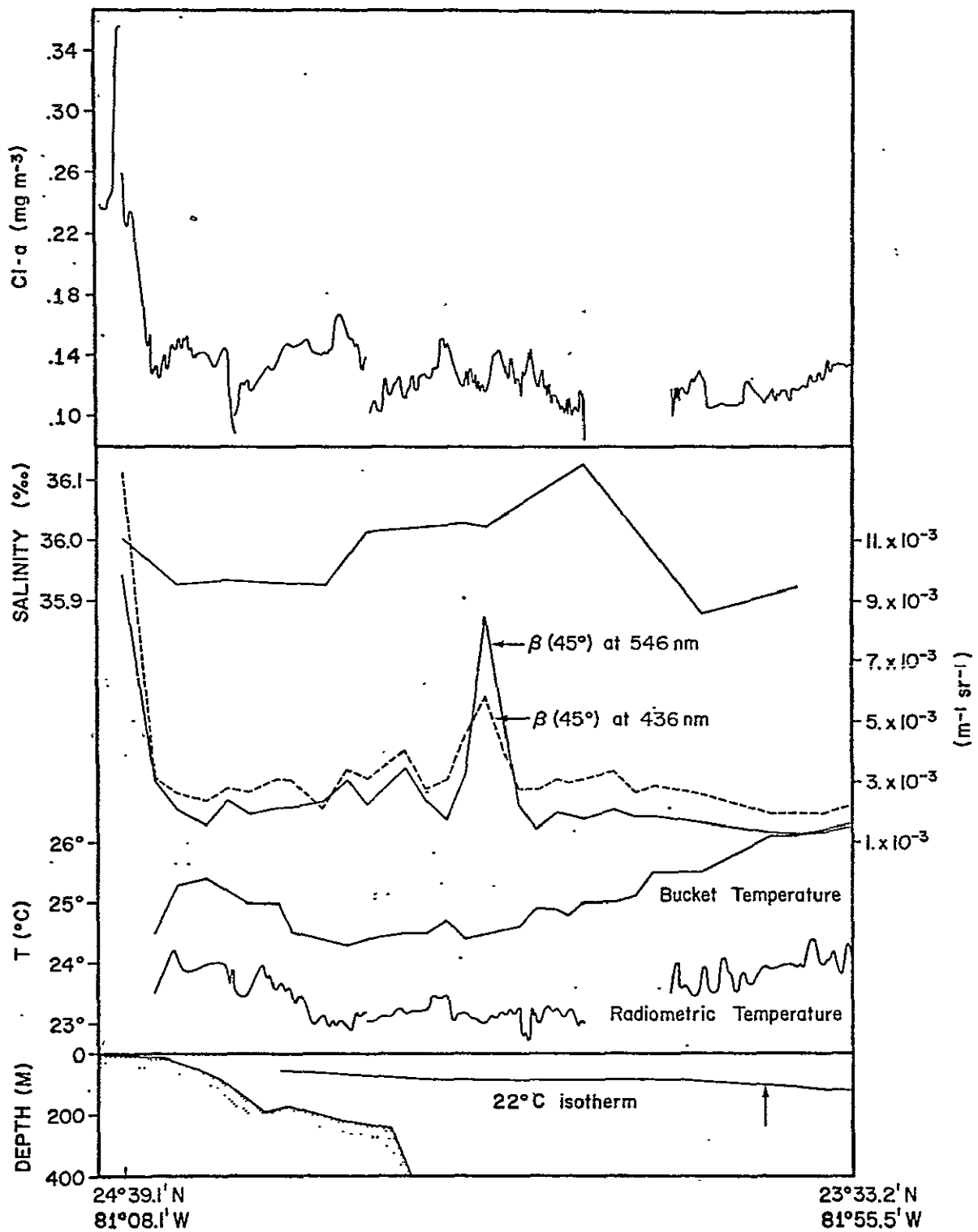
*Figure 2.1 Surface truth profiles across the Straits of Florida on
8 January 1974. The profiles, from top to bottom are: Continuous
chlorophyll-a (mg m^{-3}; discrete salinity (°/oo); discrete volume
scattering function at 45 (m^{-1}sr^{-1}); discrete thermometric temperature.
(°C); continuous radiometric temperature in 10.5 – 12.5µm band (°C);
discrete depth of 22°C isotherm.*

desirability of a continuous record instead of discrete samples as a source of the profile. The high values at the northern (left hand) end of the line occur over the reefs of the Florida Keys.

In addition to the three discrete surface samples, discrete samples at various depths were obtained while stopped at two of the spectrometer stations. This was achieved by acquiring water at the various depths for filtration and measurement later with the surface samples. Times, depths and positions are given in table A.1.

b) Salinity (S°/oo)

A total of ten salinity samples were obtained while on the track-line. These were surface water samples which were bottled for measurement after the cruise. The times and positions of the salinity samples are given in Appendix A, Table A.2. The salinity profile in Fig. 2.1, which starts at 1200 GMT, is a straight-line plot of the ten values obtained.

c) Volume scattering (β)

The volume scattering function is a measure of the amount of scattering at various angles by a sample of seawater irradiated by a beam of light. In this case a single angle of 45° was measured, for a beam with a blue filter (436 nm) and a beam with a green filter (546 nm), using a Brice-Phoenix light scattering photometer. $\beta(45)$ was calculated using:

$$\beta(45°) = \frac{a}{\pi} \frac{TD}{h} \frac{D(45°)}{D(0°)} \tau \; SIN \; 45°$$

where a is the ratio of the working standard diffuser to the reference standard diffuser, TD is the transmittance of the reference standard diffuser, h is the dimension of the irradiated element, D is the deflection of the galvonometer, and τ is the transmittance of the neutral density filters.

Measurements were obtained by collecting water samples with PVC sampler bottles. A total of thirty surface samples were measured, and at five stations samples were collected at various depths. Values, times and positions appear in Appendix A, Table A.3. The curve in Fig. 2.1, which starts at 1200 GMT, is a straight-line plot of the surface values.

d) Bucket Temperatures (T_s)

As is customary, bucket temperatures were acquired at each XBT cast. Additional bucket temperatures were acquired at spectrometry stations and at samplings for scattering measurements. The curve in Fig. 2.1 , which starts at 1215 GMT, is a straight-line plot of the 28 total temperatures obtained. See Appendix A Table A.4 for values, times

and positions.

e) Radiometric Temperature

A continuous sea surface temperature profile was obtained using a
Barnes, Model PRT-5, precision radiometric thermometer. This radiometer
has a special 10.5-12.5 µm filter that approximates those in the SKYLAB
multispectral scanner. The instrument's voltage output was converted
to temperature based on a calibration performed in March, 1974. The
profile in Fig. 2.1 begins at 1215 GMT. The large gap in the temperature
profile matches the gap in the Cl-a profile and exists for the same
reason.

·f) Expendable Bathythermograph (XBT)

A total of 23 XBT casts were made using the Sippican XBT system with
450 m probes. These casts provided the information to plot the depth
of the 22°C isotherm. The point where the 22°C isotherm crosses the
100 m depth (arrow in Fig. 2.1) is taken to mark the zone of maximum
horizontal velocity shear of the Gulf Stream. This happened at
23° 40.9' N, 81° 51.0' W, about 57 km north of the coast of Cuba. See
Appendix A, Table A.4 for times and positions.

2.3 SPECTROMETER DATA

The spectral signature of the ocean and the sky at various points
along the trackline was measured in the visible range of light. The
vessel was stopped for the spectrometry stations; six stations were
occupied for a total of 25 spectra. Table 2.1 shows the times and
positions of these stations. A detailed discussion of the instrument,
data reduction and wavelength calibration follows.

a) Instrument

The instrument was a Gamma Scientific, Model 2400 SR, spectro-
radiometer in a special watertight case. The Model 2400 SR scans in a
wavelength range of 350 to 750 nanometers (nm) by rotating a high efficiency
diffraction grating which faces a narrow aperture slit. It has a wave-
length accuracy of +2.5 nm. For this experiment the instrument was set
to scan from 375 to 725 nm with a Wratten 2b filter installed over the
entry slit. This filter effectively cuts transmission below 400 nm,
insuring that the results would not contain secondary diffraction return.
An opal glass diffuser plate was used as a cosine (Lambertian) collector;
all measurements are irradiances. The data were recorded on a dual
channel strip chart recorder.

b) Data Reduction

Fig. 2.2 is an example of a typical spectral scan. It is a
scan of ocean upwelling light from the station at 2210 GMT (see Table
2.1). The dashed curve with the many peaks is the original unsmoothed·

TABLE 2.1

Spectrometry Stations

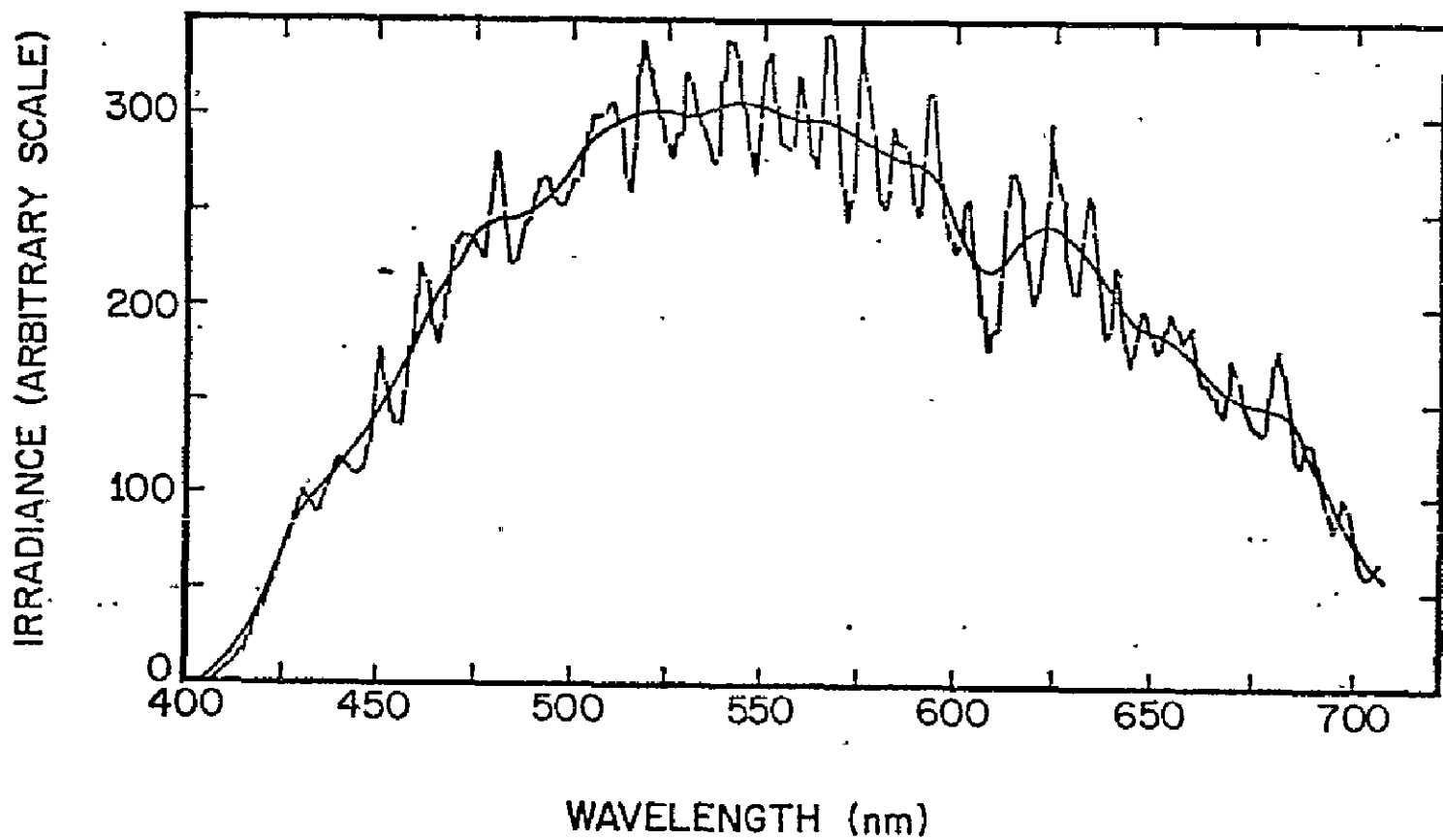| Time (GMT)	Position		Solar Zenith Angle	No. of ocean spectra	No. of sky spectra
1406	24° 38.9 N	81° 08.0 W	64°	3	1
1603	24° 30.7 N	81° 16.3 W	51°	3	2
1815	24° 19.1 N	81° 27.3 W	47°	3	2
1956	24° 08.1 N	81° 34.6 W	56°	4	1
2100	24° 04.0 N	81° 37.0 W	65°	2	0
2210	23° 58.8 N	81° 40.4 W	76°	3	1

Figure 2.2 *Example of upwelling spectral irradiance before (broken line) and after (solid line) filtering, to eliminate the effect of ocean surface glitter variations due to surface waves.*

data. The peaks are due to the changes in the angle of the water surface relative to the instrument as waves pass underneath. This imposes a fairly regular periodic variation over the general trend of the spectral return; all of the spectra acquired on this cruise showed this variation to some extent. It is necessary to remove these peaks if the data are to be useful.

Digital low-pass time series filtering techniques were used to give the spectra the smooth appearance shown by the solid curve in Fig. 2.2. These techniques, to be explained in some detail below, permit an objective filtering of the unwanted periodicities with a minimum loss of significant data trends. The filtering was performed on a UNIVAC 1108 using the FESTSA (Herman and Jacobson, 1975)software system at the Atlantic Oceanographic and Meteorological Laboratories.

The spectra were digitized off the strip chart at an interval of 20 points per inch, which was sufficiently fine to retain the shape of the original traces. For the trace in Fig. 2.2, this provided 248 data points. As different wavelength drive speeds were used on different stations, this number varied from scan to scan.

In order to choose a filter that successfully removes high frequency energy with a minimum loss of significant trends, it is important to identify the periods of the high frequency signals. Fig. 2.3 contains a plot (light, broken line) of the relative strengths of various periodicities of the spectrometry scan shown in Fig. 2.2. This is a power spectrum of the spectrometry scan using TUKEY's method (see Herman and Jacobson, 1975). One can see strong periodicities at approximately 6,7,9,20 and 30 data points per cycle. These are the dominant high frequency signals which give the original scan in Fig. 2.2 its sawtooth appearance.

The response of the filter chosen to remove these high frequency signals is shown by the heavy, solid curve in Fig. 2.3. This response is in terms of a ratio of the contribution various frequencies make to the form of the original trace, to the contribution the same frequencies are allowed to make to the form of the filtered result. Thus in the example chosen, no contribution is allowed for periods smaller than about 9 data points per cycle (10 nm), full contribution is allowed for periods greater than about 90 points per cycle (100 nm), and half contribution are allowed at about 25 points per cycle (30 nm), which was the longest period of the major peak in Fig. 2.3.

In general, all filters were chosen to remove the short period (high frequency) signals in the same way. Power spectra of different spectrometry scans did not always closely resemble each other however, and each filter had to be chosen on the basis of an individual inspection of each scan.

c). Wavelength Calibration

Irradiance and wavelength are indicated by separate voltage outputs. The wavelength voltage is produced by a potentiometer directly
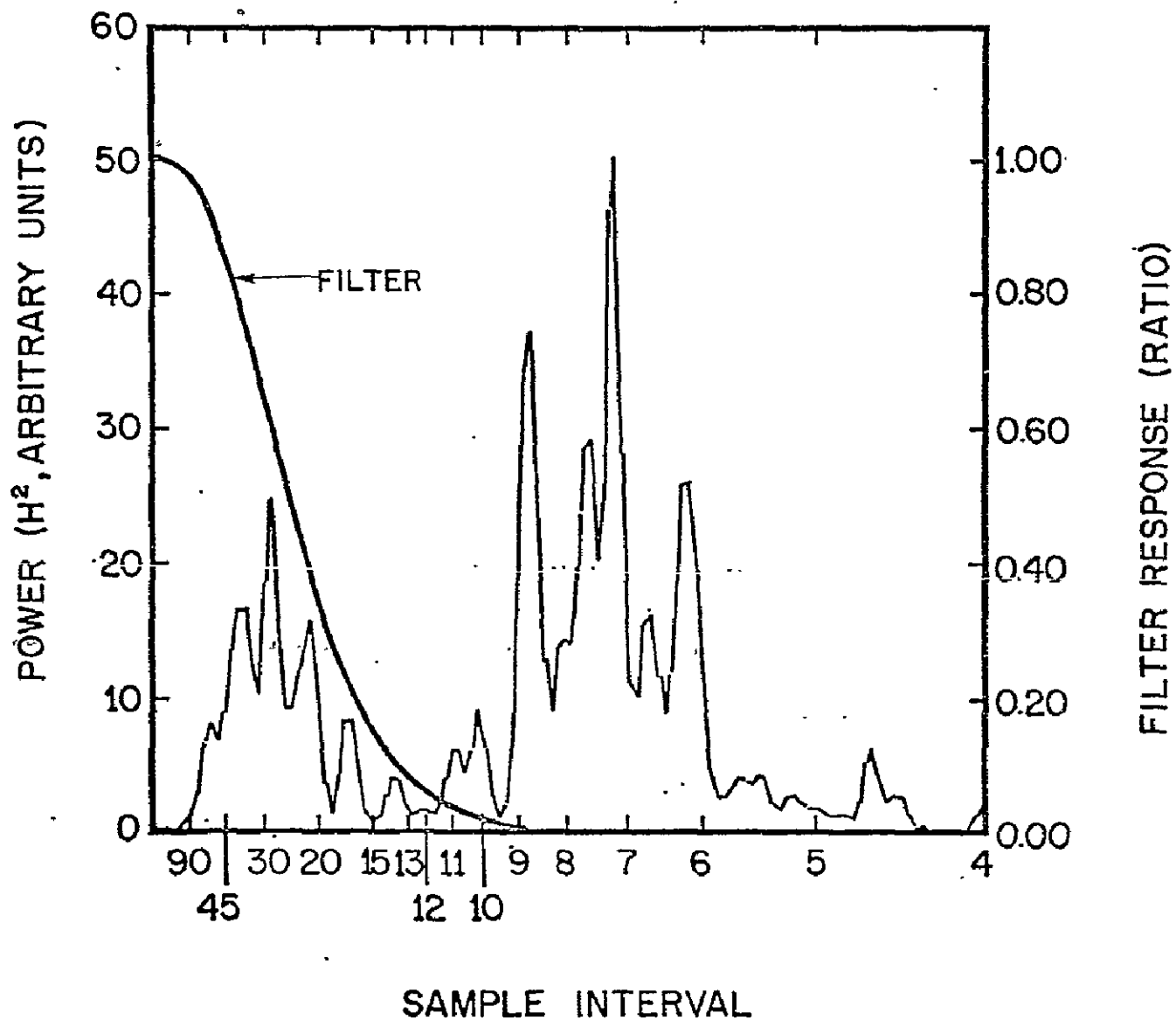
Figure 2.3   Power spectrum of upwelling spectral irradiance shown in Figure 2.2.   The narrow line is the high frequency motion caused by surface waves reflecting specularly; the heavy line is the response of the Fourier filter to low-pass the data.

connected to the diffraction grating, voltage varying with angle. In addition, an inscribed wavelength scale is connected directly to the potentiometer. Thus it is possible to compare the voltage of the wavelength output as recorded by whatever strip chart recorder is used with the wavelength indicated by the scale. Such a comparison was performed on the strip chart recorder used during the cruise, and is the basis of the wavelength calibration employed for this data. The drift free nature of the grating-scale design permits this type of calibration.

Recorder outputs were compared with scale readings at 5 nanometer intervals over the entire wavelength range used in this experiment. A third-order polynomial was fitted to the resulting numbers to obtain an equation giving wavelength in terms of the position within the spectra on the time axis of the strip chart. This form of equation was chosen because it does not require a fixed number of data points for all spectra; the only requirement is that the digitizing interval remain constant.

Comparison of this calibration with known spectral lines indicates the calibration is within 3 nanometers of true wavelength over the whole range of visible light.

3. PHOTOGRAPHY

The use of color photographs to measure phytoplankton concentrations in natural waters is based on the argument that the photographic material responds in a quantitative, reproducible manner to the variance in the light field of the water. The variance is associated in a fixed manner with the concentration of the phytoplankton, its distribution with depth, and with its species and nutritive history. For a number of years there have been applications of these variance techniques to remote sensing of the ocean (e.g. Baig and Yeutsch, 1969; Mueller, 1973). The SKYLAB experiments provided the opportunity to extend some of the techniques developed from laboratory tanks and low-level aircraft flights to synoptic mesoscale coverage. The field program (section 2.1) was to provide surface truth for the variance analysis; the SKYLAB photography was to provide the photographic products.

3.1 Measurements

A photograph is merely the record of the integral of the intensity of the illuminant falling on a subject and the reflectivity of the subject. In a color-photograph a third variable is introduced in the spectral properties of both the illuminant and the subject. A color photograph is satisfactory if it produces, in a viewer's eye, a response similar to that produced by the actual subject. The satisfactory spectral response brought about by the color photograph is a result of the eye's inability to distinguish between a pure spectral source of light and a mixture of such sources. A color photograph does not produce in each pixel (picture element) the exact spectral reflectivity of the corresponding spot of the subject (with the exception of a subject which is
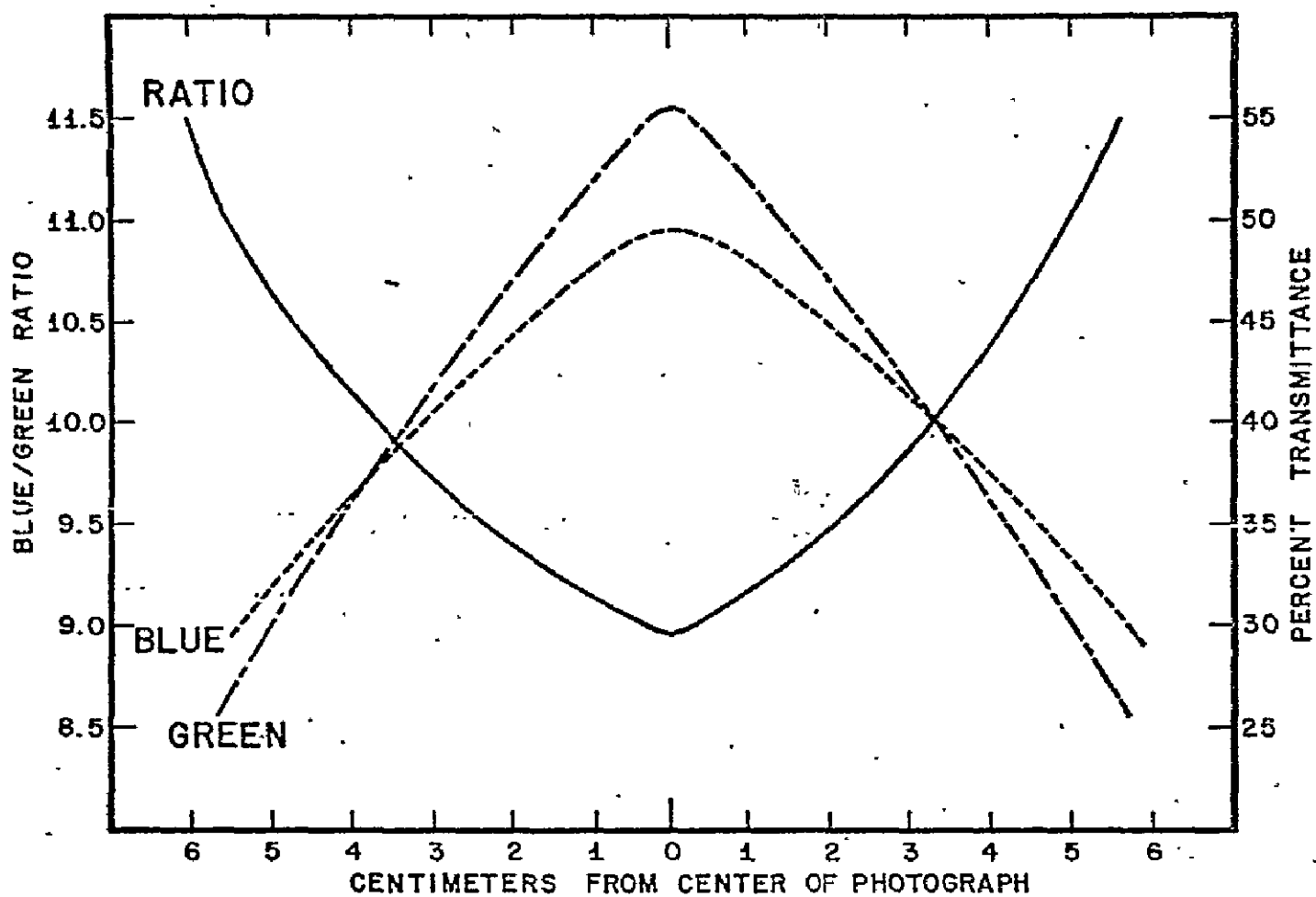
-12-

Figure 3.1 Example of the effect of vignetting in aircraft film data on the percent transmittance of blue (450 nm) and green (550 nm) light, and on the blue/green ratio. Aerial color positive film was used in the RC-8 camera.

itself a color photograph). Instead the photograph produces in each pixel a mixture of three colors which the eye perceives as a single color, and it produces only these three colors: this is called a "metameric" match.

A color can be thought of as a vector in n-space, with pure light as the origin. An infinity of coordinate systems may be created around this vector, but once one of the coordinate axes is fixed the others also become fixed. Common varieties of color films need only three colors to reproduce the variety of colors seen in the real world. To the eye these colors look like yellow, magenta, and cyan (blue-green). These colors are the coordinate axes of the color space. Every other color is an unique combination of these three primary colors. If the subject is composed of two different colors then the eye will perceive it as if it were a single color. The eye in this case performs the metameric match. A color photograph will do the same. If the color of a subject is changing then the change may be noted as differing quantities of the three dyes in a color photograph of the subject.

The utility of monitoring the changes in dye concentration of a color photograph can be carried a step further. It has been shown that, provided the continuous spectrum of the subject has previously been measured, the dye concentrations can be used to generate a new spectrum--- without re-measuring the spectrum (Baig and Yentsch, 1969). The new spectrum must have been part of a "training set" of spectra for which the color photographs exist, or must be any combination of the original training set spectra. Then, through a multivariate analysis and regression technique, a synthetic spectrum can be generated using only the dye concentrations. The technique is especially useful when the concentration of one of the components of a mixture is changing. Tank (Baig and Atwell 1975) and low-level aircraft flights (Baig, 1973) have amply demonstrated that phytoplankton concentration in natural waters can be easily and accurately measured with the technique. If the spectra of the phytoplanktors are not of immediate interest then the multivariate reduction is not necessary. The problem then reduces to a correlation between the concentration of phytoplankton in a training sample and the variation in the dye concentrations in the color photograph.

3.2 Data Analysis

The first photographs to be analysed were the 9" color transparencies from the aircraft serial cameras. On a number of frames there were subjective color differences. However, similar differences were noted on frames in which the color of the subject area would have been expected to be uniform. A densitometric analysis of one of these frames revealed a variable blue/green ratio as a function of radial distance from the principal point. These data are presented graphically in Fig. 3.1. Attempts to use these data to "correct" data from other frames of aircraft transparencies were not successful. This vignetting problem was so severe that the images were displayed on the non-linear portion of the film's D-log e curve. This introduced an unknown non-linear error which

could not be corrected without an in-flight calibration with targets of known spectral response.

Because the scale of the satellite photos is so much smaller than that of the aircraft photos, discontinuities such as fronts and eddies are recorded in only a small area of the photo. By comparison, similar elements have to be recorded over large areas of single aircraft photos, or even in a sequence of such aircraft photos. The practical effect of this scale difference is that variations in film density related to position on the photo can be ignored where the area of interest only covers a small area of the photo. Of course comparisons between areas widely scattered over the photo are still subject to the problem of spatial density in the photo.

All of the pertinent SL-4 duplicate films were analysed on a hybrid transmissometer. The light table and associated apertures, filters, and diffuse acceptor are from a Welch Denischron densitometer. The light sensor and associated electronics are a Gamma Digital Photometer. The transmission of each of the three color filters and the white light setting was calibrated with a non-silver standard step wedge traceable to N.B.S. standards. Such a step-wedge is a better approximation to the actual attenuation characteristics of color film than the usual silver grain step wedges. This is because color films do not have any silver in the final image, depending instead on dye densities for attenuation of the illuminant. Data in the following paragraph are reported as the percent fraction of transmitted light rather than as density, as transmission ratios will have a more meaningful interpretation than density ratios. Standard deviations (σ) follow each ratio.

The first area analysed was a plume of water off the coast of Cuba, in frame 97, roll 64 SL-4, near reseau #8 (Fig. 3.2). The average Blue/Green transmission (B/G) ratio is 5.9, $\sigma \pm 0.1$. Just to the left of the interface of this plume with the Gulf Stream water the B/G ratio changes to 7.0, $\sigma + 0.1$: in the Gulf Stream water. In frame 98 a similar plume on the Florida Keys side of the Gulf Stream has a B/G ratio of 6.0, $\sigma + 0.1$, while the Gulf Stream water immediately to the right of the plume has a B/G ratio of 6.8, $\sigma + 0.1$ (Fig. 3.3). This particular plume shows in three frames, 97, 98, and 99. The B/G ratios for the plume are 5.5, 6.0, and 6.2, respectively, the B/G ratios for the Gulf Stream water adjacent to the plume are 6.3, 6.8 and 7.1, respectively. Thus, while the absolute values of the ratio are changing, the difference between the plume ratio and the Gulf Stream water ratio is nearly constant from frame to frame.

Both filtered panchromatic films SO-022 showed some apparent density changes in the same areas as those in roll 64. Roll 65, filtered to pass 0.6 to 0.7 micron light showed a transmission change from 40.0×10^{1} to 34.0×10^{-1} on going from the plume off Cuba to adjacent Gulf Stream water. Roll 66, filtered for 0.5 to 0.6 micron light showed no transmission change between these two areas, both noted as 34×10^{-1}.
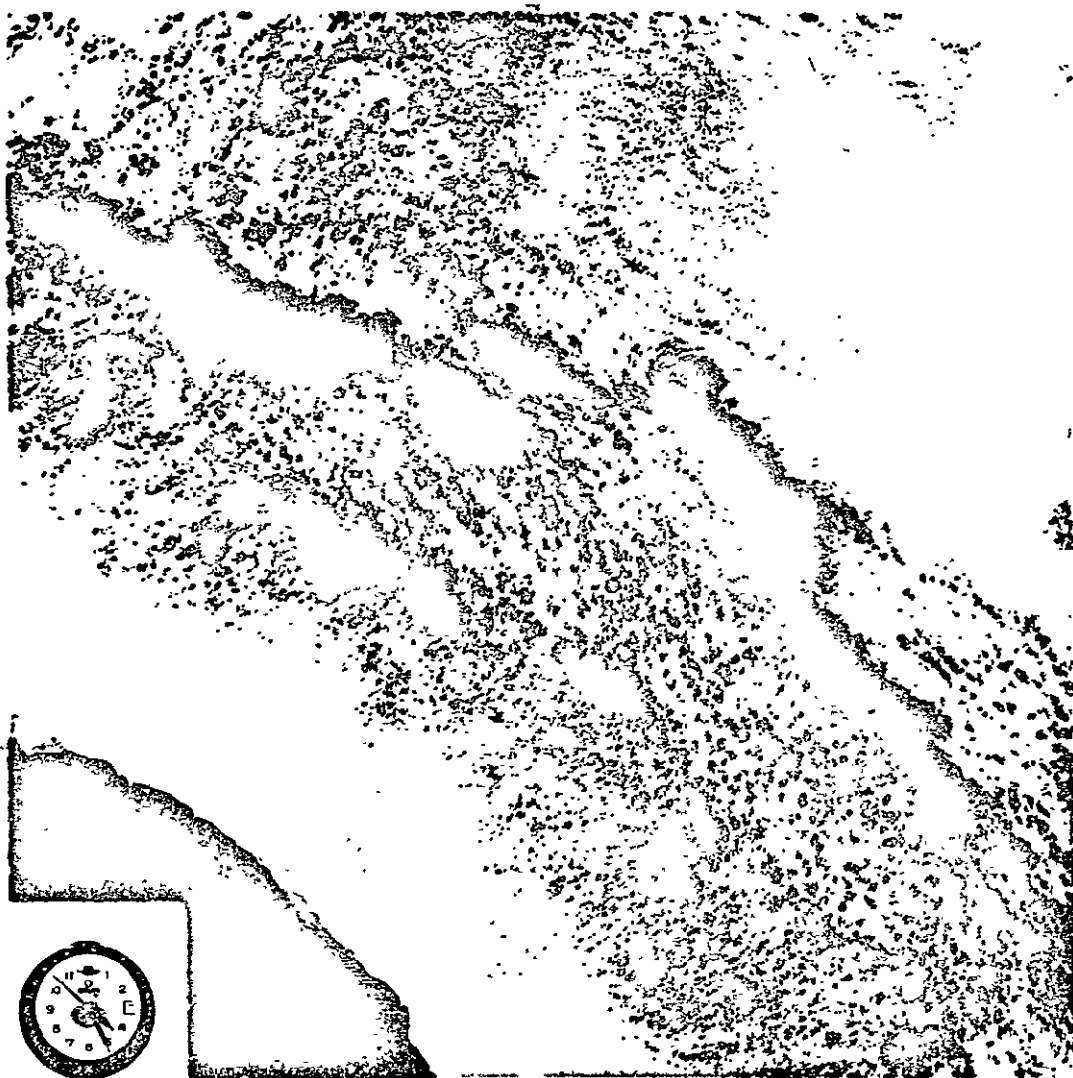
Figure 3.2 S-190B panchromatic (SO-022) photograph of the Straits of Florida and the northern coast of Cuba. The box in the lower left brackets the anticyclonic front of the Gulf Stream, and defines the area where densiometric measurements were made.
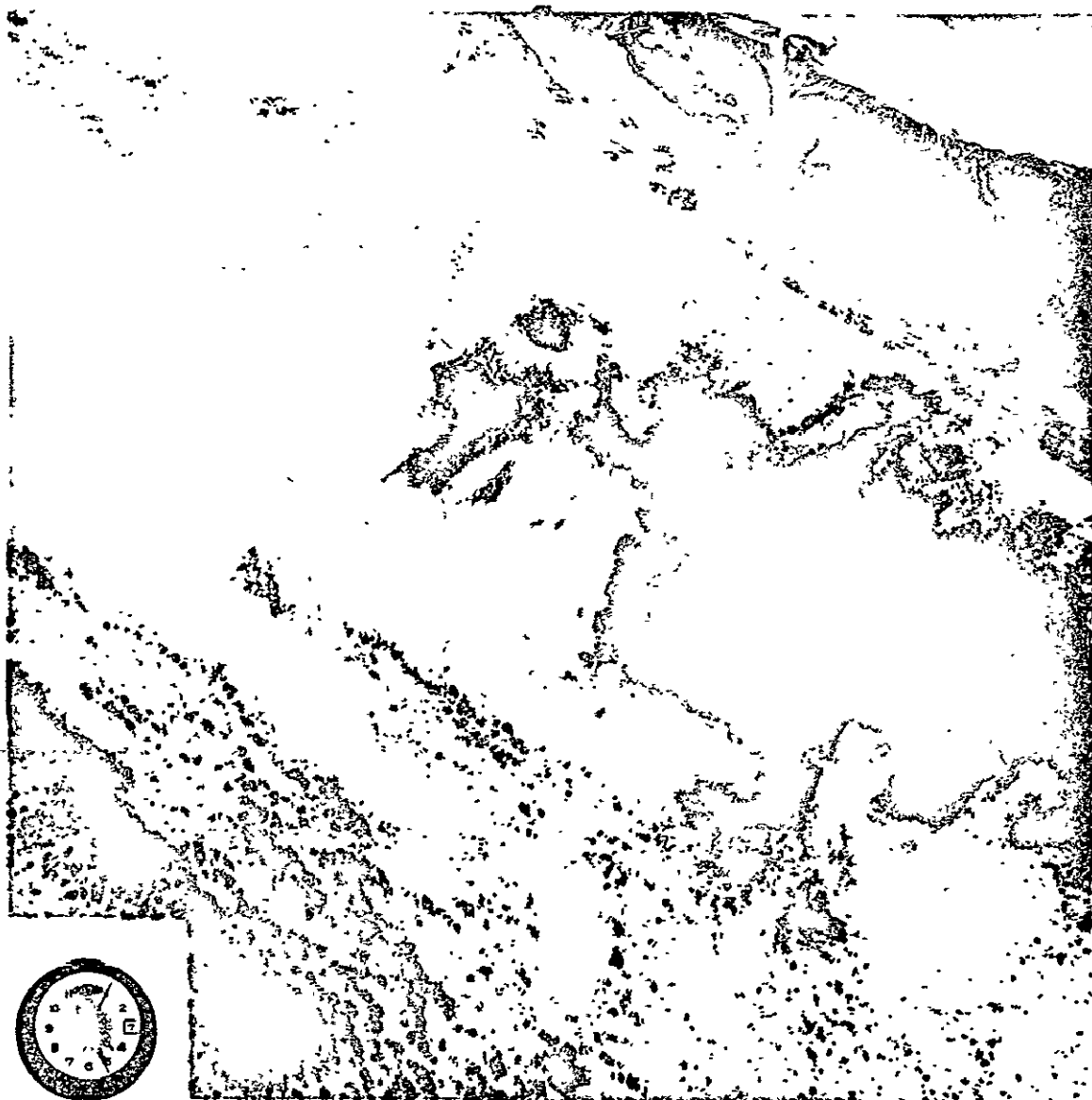
*Figure 3.3 S-190B panchromatic (SO-022) photograph. of the Straits
of Florida and the western Florida Keys. The box in the upper left
brackets a plume of water from Florida Bay, and defines the area
where densiometric measurements were made.*

Neither of the two b/w I.R. films showed any transmission differences among the areas analyzed. The color I.R. film did show some differences which are considered to be statistically significant. The plume off of Cuba showed a B/G ratio of 7.0, while adjacent Gulf Stream water showed a ratio of 7.5. The plume off the Florida Keys showed a B/G ratio of 8.5, while across the interface of the Gulf Stream water showed a ratio of 7.2. It should be noted that the B/G ratio of the color infrared film is really a ratio of the green to visible red radiation.

The conclusions which can be drawn from this limited data set are that a significant variation in ocean color can be observed by changes in dye concentrations in color photographs of the scene. By considering the surface truth the evidence tends to favor the variation in suspended chlorophyll as the most probable cause of the color variation.

3.3 Discussion

It is immediately apparent from the data that the transmission ratio technique is a useful means of analyzing variations in color of satellite-derived photography. At the same time the data might have been more useful had certain precautions been taken. Reference is specifically made to the aircraft-derived photography. To achieve a flat spectral response across the film the associated optics should have been fitted with anti-vignetting filters. The space craft cameras suffered to a lesser extent with the same problem. In this case each of the associated optics had been calibrated so that the error in transmission was known. There is however, no indication that such care was taken in preparation of the subsequent duplicate images. While care was taken to ensure that duplicate grey scales were reproduced at the same levels as those on the on-board films, apparently no account was taken of the variation in illumination across the print head of the printer. All of these problems taken together substantially reduce the possible inter-comparisons that might have been attempted.

The photographs in Figs. 3.2 and 3.3 are both S-190B products which have been enhanced by printing on high contrast film. Exposure levels were set to saturate the details in the non-oceanic features. This is a trial and error technique that extracts markedly more low radiance level information. The change in texture marking differing sea states in Fig. 3.2 is not measureable using the densitometer technique, but it is clearly noticeable to the eye. The boundary between the two levels of radiance is probably the anticyclonic edge of the Florida Current. The detection of the features in Figs. 3.2 and 3.3 by the S-192 scanner is discussed in section 5.

4. SPECTROMETER EXPERIMENT

The SKYLAB S-191 steerable spectroradiometer was to be used in this experiment to study changes in the visible (0.4-0.7 μ m) and infrared (7.0- 14.0 μm) spectra of the ocean across the current's cyclonic boundary. The plan was for the crew to acquire a cloud-free oceanic area with the

S-191 looking 45° forward of nadir, and track that site until 0°. Thereafter, the spectroradiometer was to be locked into nadir viewing across the cyclonic front and up into the waters of Florida Bay.

The experiment proved to be not very successful for several reasons: while the crew did as the plan said, the data acquisition camera (DAC) was turned off and the exact tracking data (angles, times, locations) were never recorded; the calibration of the S-191 infrared detectors is not known; the visible region data radiances values do not agree with theoretical or observed values reported by other investigators. The DAC problem will be discussed in this introduction, and the infrared and visible data in sections 4.1 and 4.2, respectively, below.

Location of the data is made difficult by the lack of DAC output. The voice log was the best clue to what actually was done by the crew. From the transcript of the voice tape, at 16:29:33 GMT the pilot had the S-191 set at 35° looking forward along the track, although all crew instructions were to set the S-191 target acquisition at 45°. The word "thirty five" was not clearly audible however, and the pilot may have followed the instructions sent up to SKYLAB just prior to the pass. At 16:29:35 GMT, the pilot reported tracking a clear area of water; the assigned start time was 16:29:33. The exact time of reaching nadir is difficult to tell from the voice log, however 16:30:45 is the approximate time.

The location and time of the nadir point was calculated from geometrical considerations assuming a spherical earth with a radius of 6378 km and a satellite altitude of 443 km. If the nadir angle was 45° at 16:29:33 GMT, the position of the point tracked was 23° 53'.4 N, 81°58'.0W; the time of arrival of the spacecraft over this point from the best available positioning data is 16:30:41.1 GMT, which is in good agreement with the voice log estimate. The message sent up to the crew had the finish of the tracking at 16:31:05.

The S-192 line straightened data show that the position given above is in the middle of a clear ocean area and it appears reasonable to have tracked this as the site. The vehicle was over Florida Bay at 16:30:55 according to the S-192, but the pilot commented at 16:31:10 that they were going across the Keys. This discrepancy cannot be accounted for unless the Florida Keys were observed well after the spacecraft transit.

If the above analysis is correct, then according to the ground truth data in Fig. 2.1, the Gulf Stream was probably never acquired by the S-191. The position of the 22°C isotherm at 100 meters depth indicator was 25 km SW of the point where the pilot tracked a clear area. Although the exact location of the front cannot be identified in the ship track data it appears that it was also SW of the nadir tracking point. Maul (1975) reported the mean separation between the indicator isotherm and the front to be 11 km in this area and that data further supports the contention that the S-191 did not obtain spectra in the Gulf Stream. The objective of analyzing the change in spectra

across the front cannot be accomplished with these data.

4.1 Infrared Radiance

The infrared experiment was designed to study the accuracy of atmospheric transmission models. This objective cannot be accomplished because the calibration of the infrared detector is an unknown function of wavelength (Barnett, personal communication; Anding, 1975). Several relative tests were made however, which provide some information on the atmospheric transmission model dependency, and these will be discussed below.

4.1.1 Theoretical Calculations

Emitted infrared radiation (7 $\mu m \leq \lambda \leq 14$ μm)leaving the earth passes through the atmosphere before detection at the S-191 sensor. The atmosphere modifies the infrared radiation by absorption and, to a very minor degree, by scattering. Details of the theory are given by Chandrasekar (1960) and recent reviews on its application to oceanography were given by Hansen (1972) and Maul (1973). The radiative transfer equation through an absorbing but non-scattering atmosphere is:

$$N(\theta,\lambda) = \varepsilon(\theta',\lambda)\ L\ (T,\lambda)\ \tau(\theta,\lambda)$$
$$+ \int_0^{P_s} L(Ta,P,\lambda)\ \frac{\partial\tau(p,\theta,\lambda)}{-\partial p}\ p \qquad (4.1)$$
$$+ \rho\ (\theta',\lambda)\ N_{as}\ (\theta'',\lambda)\ \tau(\theta,\lambda)$$

where θ,θ',λ'' are the nadir angle, angle of reflectance, and angle of incidence, respectively. Radiance (N) at the satellite is wavelength dependent, and is a function of the surface blackbody radiance (L), the emissivity of the surface (ε) and the transmittance of the atmosphere (τ); these three parameters describe the absorption of emitted blackbody radiation by the atmosphere. The second term in the equation, the integral term, describes the atmospheric (a) modification of the radiance as a function of pressure (P). The third term describes the contribution of the reflected (ρ) atmospheric radiance at the surface (N_{as}), again as modified by transmittance.

The theoretical calculations discussed herein are an extention of the model used by Maul and Sidran (1973) which uses the transmissivity data of Davis and Viezee (1964). The area of interest is the 10.5 - 12.5 μm band which is used on many spacecraft including the SKYLAB S-192 multispectral imager. In this spectral interval $\varepsilon > 0.99$ at low nadir angles; hence $\rho(=1-\varepsilon)$ is very small and equation 4.1 may be written

$$N(\theta) = \int_0^\infty \phi(\lambda)\ L\ (Ts,\lambda)\ \tau(\theta,\lambda)d\lambda$$
$$\int_0^\infty \int_0^{P_s} \phi(\lambda)\ L\ (Ta,p,\lambda)\ \frac{\partial\tau(p,\theta,\lambda)}{\partial p}\ dpd\lambda \qquad (4.2)$$
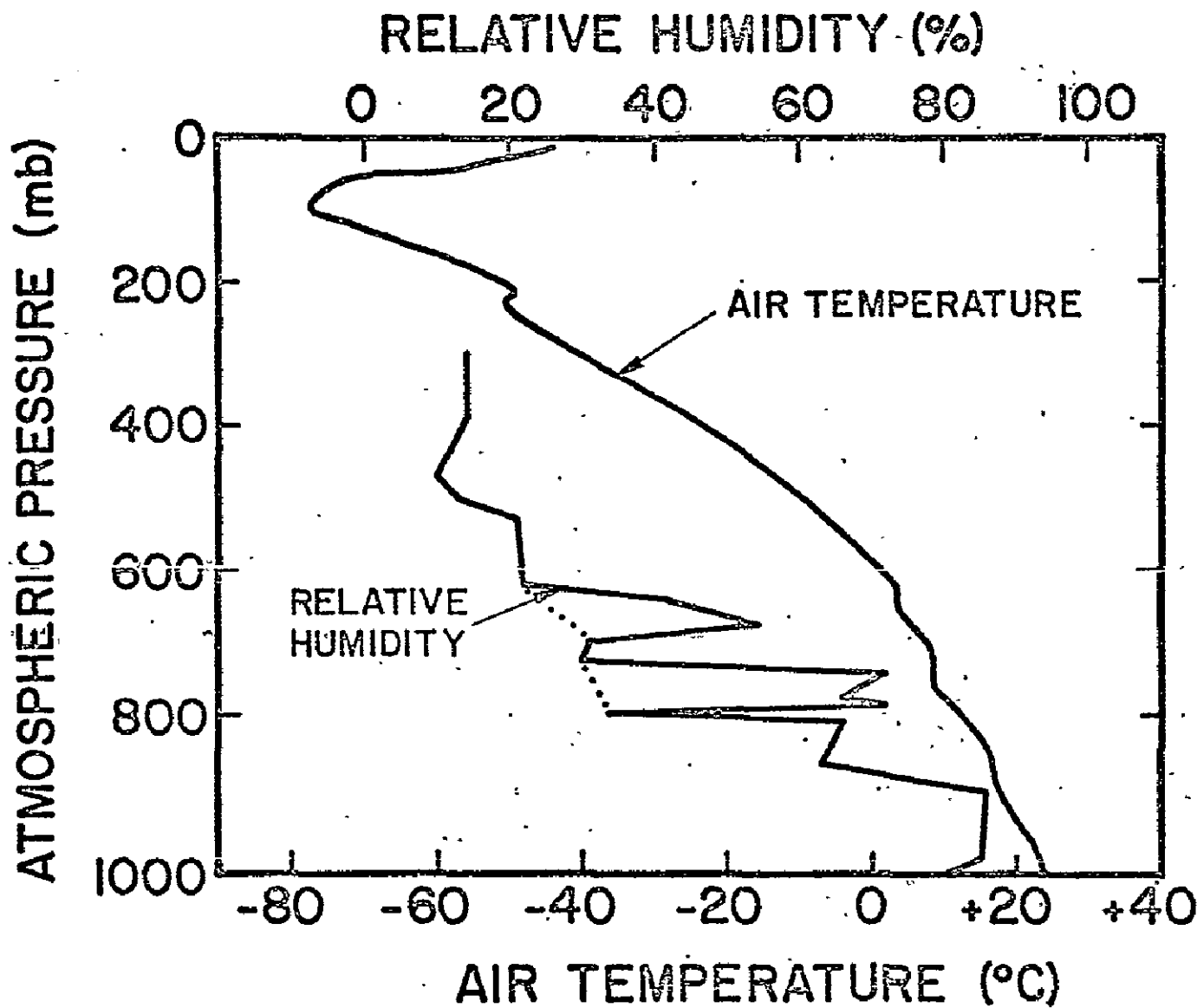
Figure 4.1 Vertical profiles of atmospheric pressure and relative humidity taken at the time of SKYLAB transit. The dotted lines on the relative humidity profile are the cloud-free estimate of atmospheric moisture.

The filter function (ϕ) is zero outside the interval discussed above. The radiance may be converted to equivalent blackbody temperature by inverting the Planck equation (L) which has been integrated over the same $10.5 \leq \phi \leq 12.5$ interval.

The calculations were carried out on the AOML computer. A special radiosonde was released by the Key West office of the National Weather Service at the time of SKYLAB transit (see Fig. 4.1). Before computing the radiative transfer from a radiosonde, the data must be inspected to insure that no clouds are in the path of ascent in order to compute a cloud-free radiance. Clouds are readily identified by their characteristically high relative humidity and isothermal temperature. There is evidence of clouds in the data in Fig. 4.1, and calculations were made to test the effect of clouds.

Two cloud layers are in evidence, one centered at 744 mb and one centered at 671 mb. Clouds are characterized by a sudden increase in relative humidty and a small (near zero) lapse rate. An equivalent clear sky estimate is made by assuming the clouds are absent; the estimated relative humidity profile in the clouds region is given by the dotted curve. The calculated equivalent blackbody temperatures for T_s 298.15°1C are:

Wavelength	Observed (Appendix B)	Cloud-free Equivalent
11µm	293.22° K	293.85° K
12.5µm	290.46° K	291.28° K

The differences in this case are small, 0.63° K at 11µm, and 0.82° K intergrated over the 10.5-12.5µm region where the S-192, NOAA-4/5 and SMS-1/2 observe. Other experience with this type of cloud-free equivalence has been as high as 5° K over the Gulf of Mexico.

4.1.2 Comparison of S-191 and Models

As stated in section 1.3, the wavelengths chosen for the two – channel technique,(Anding and Kauth, 1970) of atmospheric correction depend on the radiative transfer model. SKYLAB was to be used to study that question but since the calibration of the S-191 infrared detector is unknown, the problem cannot be investigated.

The mean sea surface temperature along the trackline was 25.0°C. This value has been used in the calculations shown in Fig. 4.2. The Davis and Viezee (1964) model does not include absorption due to the ozone molecules which show up as a maximum at 9.6µm in the S-191 observation. The comparison shows that ozone does not affect the 10.5-12.5µm window and hence is not a factor in the S-192 infrared scanner data. At 11.0µm, the apparent difference between the observed and calculated equivalent blackbody temperature (T_{BB}) is 3.5°C. This seems to be the approximate error estimate of other SKYLAB investigators (personal communications), but no conclusions can be drawn.
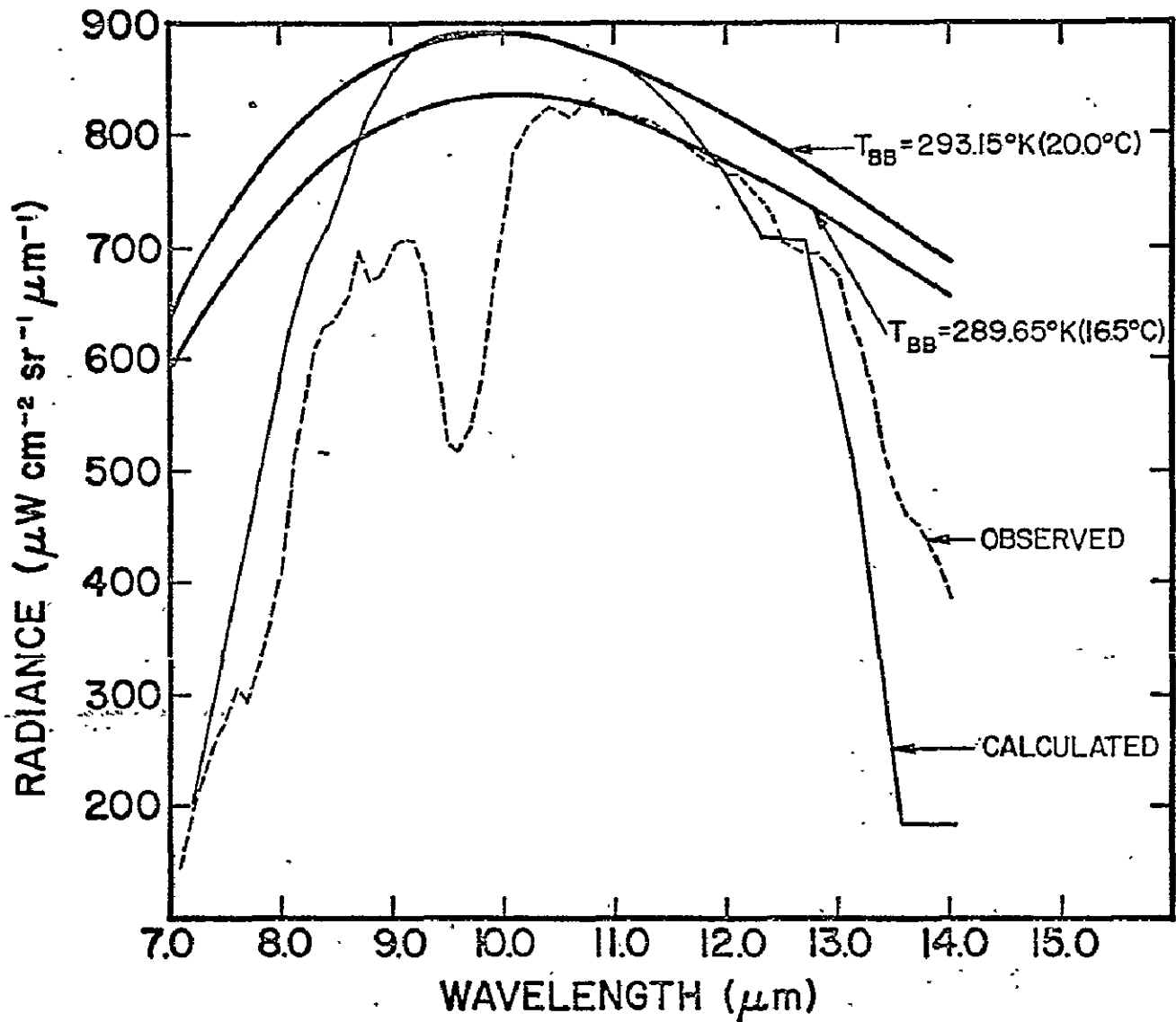
Figure 4.2 Spectral infrared radiance observed by the S-191 spectroradiometer (dashed line), and calculated by the ozone excluding model of Davis and Viezee (fine solid line). Heavy solid lines are blackbody curves.

Since the calibration uncertainty is wavelength dependent, the data at 11 μm were studied to determine the shape of the nadir angle dependence curve. In the lower half of Fig. 4.3 is a least-squares fourth order polynomial fit to all the observed radiances as a function of time (dashed line). Since the same ocean spot was to be tracked, radiance should be a function of nadir angle up to 16:30:45 GMT. The maximum on this curve (arrow) is at 16:30:19. The upper curve is the theoretical calculation using equation 4.2 for the same atmosphere in Fig. 4.1 and for T =25°C. Nadir angles were computed using a start time of 16:29:35 GMT (45°) and a stop time of 16:30:45 GMT (0°) following the discussion in section 4.0. The match in the curves maxima would be approximately coincident if the tracking started with a 37° nadir angle, which is in agreement with the voice tape transcript.

The S-191 spectroradiometer uses a series of detectors which cover a segment of the spectrum. In some regions these overlap and ambiguity often exists as to which detector to use. In the sections to follow, those detectors (channels) chosen were as recommended in the NASA reports on instrument performance. It is suggested that only that data which is well calibrated be reported to non-instrument engineering investigators in the future.

Barnett (personal communication) cautioned against the use of radiometer channel A1 in the S-191 (see again Fig. 4.3) Accordingly a second fourth-order polynomial (solid line) was fitted to the channel A6 data only. The rms spread of the radiance about this polynomial is 4.48 μW cm^{2} sr^{1} μm^{1}. This corresponds to a noise equivalent temperature difference (NEΔT) of $\pm$ 0.3°K at 289.65°K. Since the atmospheric attenuation tends to diminish surface gradients, this results in a calculated NE ΔT of approximately $\pm$ 0.6°C in T_S for this model at 11 μm on this day. The equivalent blackbody temperature at the maximum in the polynomial is 16.5°C at the top of the atmosphere. This implies a temperature correction of 8.5°C which is not unreasonable for a tropical winter atmosphere whose precipitable water vapor is 3.6 cm (cf Maul and Sidran, 1973).

4.2 VISIBLE RADIANCE

The visible experiment was designed to study the accuracy with which spectral changes across oceanic fronts can be observed and interpreted from satellite altitudes. Unfortunately, the strongest front expected in the experiment area was missed by the S-191 so this objective, as discussed before, cannot be accomplished. However, during the course of this work, a theoretical technique for recovering the "ocean color spectrum" through the atmosphere was developed. This is discussed in detail below and an attempt is made to compare the predictions of the theory with the S-191 data and the associated ground truth.

4.2.1 Theoretical Calculations

It is clear that the full potential of oceanic remote sensing from space in the visible portions of the spectrum can be realized only if
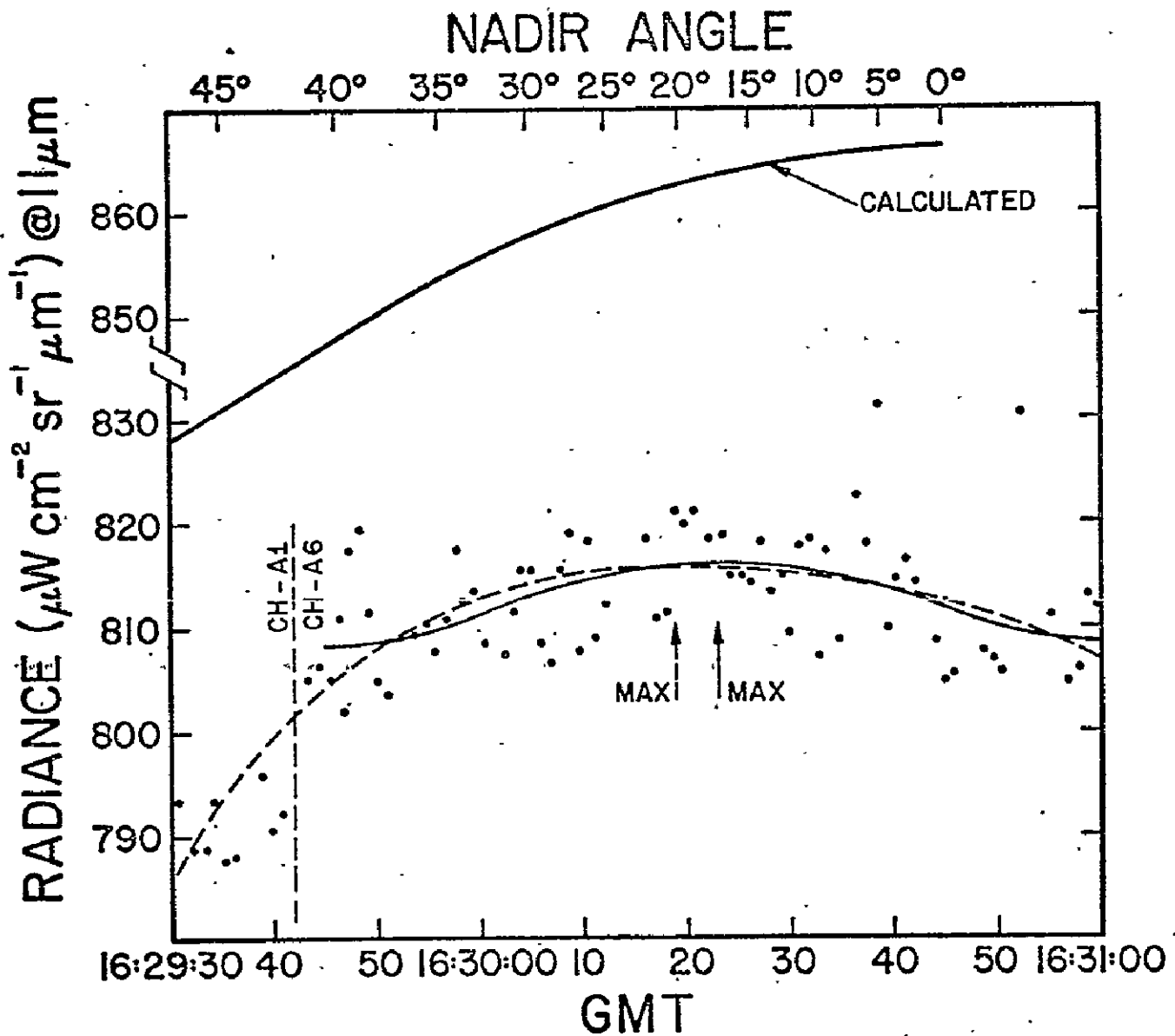
Figure 4.3 Radiance at 11μm as a function of nadir angle of the same ocean spot as tracked on the S-191 (dots). Channel A1 data to the left of the vertical dashed line; channel A6 to the right. Dotted line is fourth order polynomial fit to all data; fine solid line is fourth order polynomial fit to A6 data only. Heavy solid line is the calculated nadir angle dependence.

the radiance which reaches the top of the atmosphere can be related to
the optical properties of the ocean. To effect this, the radiative
transfer equation must be solved for the ocean-atmosphere system with
collimated flux incident at the top of the atmosphere. In such calcula-
tions the optical properties of the ocean which must be varied are the
scattering phase function ($P_0(\theta)$) and the single scattering albedo
(ω_0; defined as the ratio of the scattering coefficient to the total
attenuation coefficient). Furthermore, unless the ocean is assumed to
be homogeneous, the influence of vertical structure in these properties
must be considered. To describe the cloud free atmosphere, the optical
properties of the aerosols and their variation with wavelength and
altitude as well as the ozone concentration must be known. Considering
the ocean for the present to be homogenous, the radiance at the satellite
can be related to the ocean's properties by choosing an atmospheric
model and solving the transfer equation for several oceanic phase functions
and ω_0's at each wavelength of interest. The number of separate computa-
tional cases required is then the product of the number of phase functions,
the number of values of ω_0, and the number of wavelengths. Even if the
multi-phase Monte Carlo method (MPMC, Gordon and Brown, 1975) is used,
the ω_0 resolution of Gordon and Brown (1973) would require a number of
simulations equal to ten times the number of wavelengths for each
atmospheric model considered. It is possible, however, to obtain the
necessary information without modeling the ocean's optical properties
in such detail.

The model is based on an observation evident in results of
computations given by Plass and Kattawar (1969) and by Kattawar and
Plass (1972) on radiative transfer in the ocean atmosphere system,
namely, that when the solar zenith angle is small, the upwelling radiance
just beneath the sea surface is approximately uniform, (i.e., not strongly
dependent on viewing angle) and hence determined by the upwelling irradiance.
This observation is utilized in simulations of oceanic remote sensing
situations by assuming that a fraction R of the downwelling photons are
absorbed. The ocean is then treated as if there is a lambertian reflecting
surface of albedo R just beaneath the sea surface. In this case Gordon
and Brown (1974) have shown that any radiometric quantity Q_1 can be
written

$$Q = Q_1 + \frac{Q_2 R}{1-rR} \qquad (4.3)$$

Q_1 is the contribution to Q from photons which never penetrate
the sea surface (but may be specularly reflected from the surface). Q_2
is the contribution to Q from photons which interact with the hypo-
thetical "labertian surface" once for the case R=1. r is the ratio of
the number of photons interacting with the "lambertian surface" twice,
to the number of photons interacting once, again for R=1.

Using equation 4.3 any radiometric quantity can then be computed as
a function of R. Physically the quantity R is the ratio of upwelling to downwelling
irradiance just beneath the sea surface and is known as the reflectance

Table 4.1.   The Three Ocean Scattering Phase Functions

θ (deg)	KA (x10²)	KB (x10²)	KC (x10²)
0	10924	10171	9521
1	4916	4577	4285
5	573.5	534.0	499.9
10	169.3	157.7	147.6
20	29.5	29.39	29.31
30	12.56	11.95	11.42
45	3.059	3.661	4.189
60	1.092	1.577	1.999
75	0.546	0.915	1.190
90	0.344	0.661	0.952
105	0.311	0.641	0.928
120	0.317	0.732	1.094
135	0.410	0.829	1.309
150	0.492	1.017	1.618
165	0.579	1.261	1.856
180	0.617	1.357	1.999

function [R(0,-)] in the ocean optics literature (Preisendorfer, 1961). Spectral measurements of the reflectance function $R(\lambda)$ have been presented for various oceanic areas by Tyler and Smith (1970). Henceforth, $R(\lambda)$ will be referred to as the "ocean color spectrum."

A series of Monte Carlo computations have been carried out to see if an approximate simulation (AS1), using this assumption of uniform upwelling radiance beneath the sea surface, yields results which agree with computations carried out using an exact simulation (ES), in which the photons are accurately followed in the ocean as well as the atmosphere. The Monte Carlo codes used in Gordon and Brown (1973, 1974) were modified by the addition of an atmosphere. The atmosphere consisted of 50 layers and includes the effects of aerosols, ozone, and Rayleigh scattering, using data taken from the work of Elterman (1968). The aerosol scattering phase functions were computed by Fraser (NASA-GSFC, personal communication) from Mie theory assuming an index of refraction of 1.5 and Deirmendjian's (1964) "haze C" size distribution. Also, to determine the extent to which the vertical structure of the atmosphere influences the approximate simulation, a second approximate simulation (AS2) was carried out in which the atmosphere was considered to be homogeneous; i.e., the aerosol scattering, Rayleigh scattering, and ozone absorption were independent of altitude. The oceanic phase functions in the ES are based on Kullenberg's (1968) observations in the Sargasso Sea, and are given Table 4.1.

KA is roughly an average of Kullenberg's phase function at 632.8 nm and 655 nm, and KC is his phase function at 460 nm. KB is an average of KA and KC. These phase functions show considerably less scattering at very small angles ($\theta < 1°$) than observed by Petzold (1972) in other clear water areas; however, the exact form of the oceanic phase function is not very important, since it has been shown (Gordon, 1973) to influence the diffuse reflectance and $R(0,-)$ only through the back-scattering probability (B)

$$B = 2\pi \int_{\pi/2}^{\pi} P_o(\theta) \sin\theta\, d\theta.$$

In all of the computations reported here, the solar beam incident on the top of the atmospshere, is from the zenith and with unit flux. At visible wavelengths, the variable atmospheric constituent which will most strongly influence the radiance at the top of the atmosphere is the aerosol concentration, so the computations have all been carried out as a function of the aerosol concentration.

Table 4.2 gives a sample of the results comparing the upward flux at the top of the atmosphere at 400nm in the three simulation models (ES, AS1, and AS2) as a function of the aerosol concentration. N, 3 x N, and 10 x N respectively refer to aerosol concentrations in each layer of 1, 3, and 10 times the normal concentration given by Elterman. 400 nm is chosen because in the visible portion of the spectrum it is the wavelength at which the atmospheric effects are expected to be most severe. The ES case uses $\omega_o = 0.8$ and phase function KC. The values

Table 4.2: Comparison of the flux at the top of the atmosphere for the ES, AS1, and AS2 simulations.

Aerosol Concentration	ES	AS1	AS2
N	0.222 (+.002)	0.224 (+.001)	0.226 (+.001)
3xN	0.274 (+.003)	0.273 (+.001)	0.275 (+.001)
10xN	0.423 (+.004)	0.426 (+.002)	0.425 (+.002)

of R used to effect the AC computations were taken from the EC computation of this quantity, however if R is taken from

$$R = 0.0001 + 0.3244x + .1425x^2 + .1308x^3 \qquad (4.4)$$

where $x = \omega_0 B/(1-\omega_0(1-B))$ which, according to Gordon, Brown and Jacobs. (1975), reproduces the in-water reflection function for the corresponding case but with no atmosphere present, the results of the AS computations agree with those listed to within 0.2%. The numbers in the parenthesis next to each flux value represents the statistical error in the flux based on the actual number of photons collected in each case. It is seen that ES and AS simulations generally agree to within the accuracy of the computations. Notice also the excellent agreement between the As1 and As2 fluxes.

In Fig. 4A the comparison between the ES, AS1 and AS2 upward radiances at the top of the atmosphere is presented for the three aerosol models. The step-like curve in the figure is for ES, the solid circles for AS1, and the open circles for AS2, and μ_0 is the cosine of the angle between the nadir and the direction toward which the sensor is viewing. The radiances in Fig. 4.4 for the ES cases are accurate to about 3% in the range $\mu = 1$ to about 0.4, while for the AS cases the accuracy is about 1%. To within the accuracy of the computations, the three simulations again agree for all the aerosol concentrations except within the range $\mu = 0$ to about 0.3; i.e., viewing near the horizon. It is felt that these computations demonstrate that the transfer of the ocean color spectrum through the atmosphere can be studied with either the AS1 or AS2 model as long as radiances close to the horizon are not of interest. Furthermore, from the reciprocity principle (Chandrasekhar, 1960) the nadir radiance, when the solar beam makes an angle θ_0 with the zenith, can be found by multiplying the radiance $I(\mu)$ in Fig. 4.4 by μ where μ is taken to be $\cos\theta_0$. This implies that as long as the sun is not too near the horizon, the AS1 and AS2 methods of computation can be used to determine the nadir radiance at the tip of the atmosphere as a function of the ocean's properties through equation 4.4. The fact that the AS2 model (homogeneous atmosphere) yields accurate radiances is very important in remote sensing since it implies that only the total concentration (or equivalently the total optical thickness) of the aerosol need be determined to recover the ocean color spectrum from satellite spectral radiometric data.

It should be pointed out that these results also strongly suggest that $R(\lambda)$ is the quantity relating to the subsurface conditions, which can be quantitatively determined from space, and hence, is the most natural definition of the "ocean color spectrum". Moreover, it has been shown (Gordon, Brown, and Jacobs, 1975) that $R(\lambda)$ is not a strong function of the solar zenith angle (the maximum variation in $R(0,-)$ with θ_0 is of the order of 15% for $0 < \theta_0 \lesssim 60°$) in contrast with other definitions (Curran, 1972; Mueller, 1973).
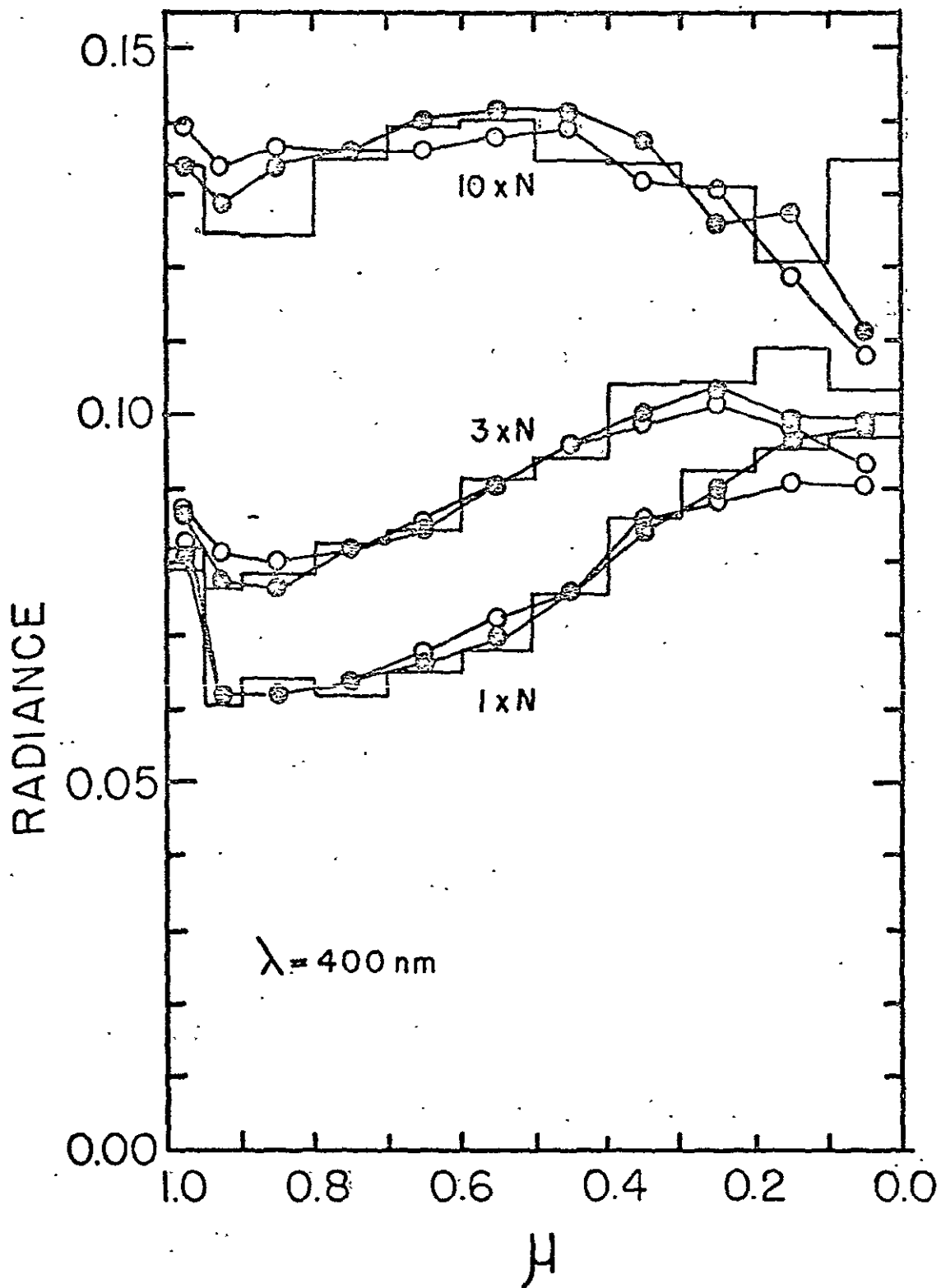
Figure 4.4 Comparison between ES (step like curve) AS1 (solid circles) and AS2 (open circles) upward radiances at the top of the atmosphere for an ocean with $\omega_0 = 0.8$ and phase function KC and an atmosphere with a normal (1xN), three times normal (3xN) and ten times normal (10xN) aerosol concentration.

The only way spacecraft data can be used to obtain information concerning subsurface conditions (such as concentrations of chlorophyll, suspended sediments, etc.) is through determination of $R(\lambda)$. [It is assumed here that the relationship between $R(\lambda)$ and the ocean constituents is well known, while in fact much work still remains to be carried out before such a relationship can be established]. This can be effected by applying equation 4.3 to radiance $I(\mu)$ at the top of the atmosphere with the sun at the zenith, which yields,

$$I(\mu) = I_1(\mu) + \frac{R\,I(\mu)}{1 - rR}$$

$I_1(\mu)$ and $I_2(\mu)$ are presented in Figs. 4.5 and 4.6 respectively for the three aerosol models discussed above as well as an aerosol free model ($0 \times N$) and a model with seven times the normal aerosol concentration ($7 \times N$). For the cases considered, $r \cong 0.5$ and since R is usually about 0.03 to 0.10 at this wavelength we can rewrite equation 4.5 approximately as

$$I(\mu) = I_1(\mu) + RI_2(\mu) \qquad\qquad (4.5')$$

so $\quad R \cong \dfrac{I(\mu) - I_1(\mu)}{I_2(\mu)} \qquad\qquad (4.6)$

Applying the reciprocity theorem to equation 4.6 it is found for nadir viewing, that

$$R \cong \frac{I_{nadir} - \mu_0\,I_1(\mu_0)}{\mu_0\,I_2(\mu_0)} \qquad\qquad (4.7)$$

where μ_0 is the cosine of the solar zenith angle θ_0. Noting again that R is $\cong 0.10$ it is seen that the difference between I_{nadir} and $\mu_0 I_1(\mu_0)$ must be small which implies that the accuracy in R will be limited by knowledge of $I_1(\mu_0)$. Since $I_1(\mu_0)$ depends strongly on the aerosol concentration, it is absolutely necessary to be able to determine the aerosol concentration if an accurate value of R is desired. Curran (1972) has suggested that this can be accomplished by observing the ocean (assumed free of white caps) in the near infrared where $R(\lambda) \cong 0$. In section 4.22 of this report, Curran's suggestion is utilized to find the aerosol concentration from the S-191 data.

Before trying to apply the relationships developed here to the S-191 spectra, there are several important implications of the theory which shall be discussed. Noting that $I_1(\mu)$ and $I_2(\mu)$ depend only on the direction of the incident solar beam, the properties of the atmosphere and ocean surface, but not R, if it is assumed these latter properties remain essentially constant over horizontal distances large compared to those over which R changes significantly, one can directly relate changes in $I(\mu)$ to changes in R. From equation 4.5'

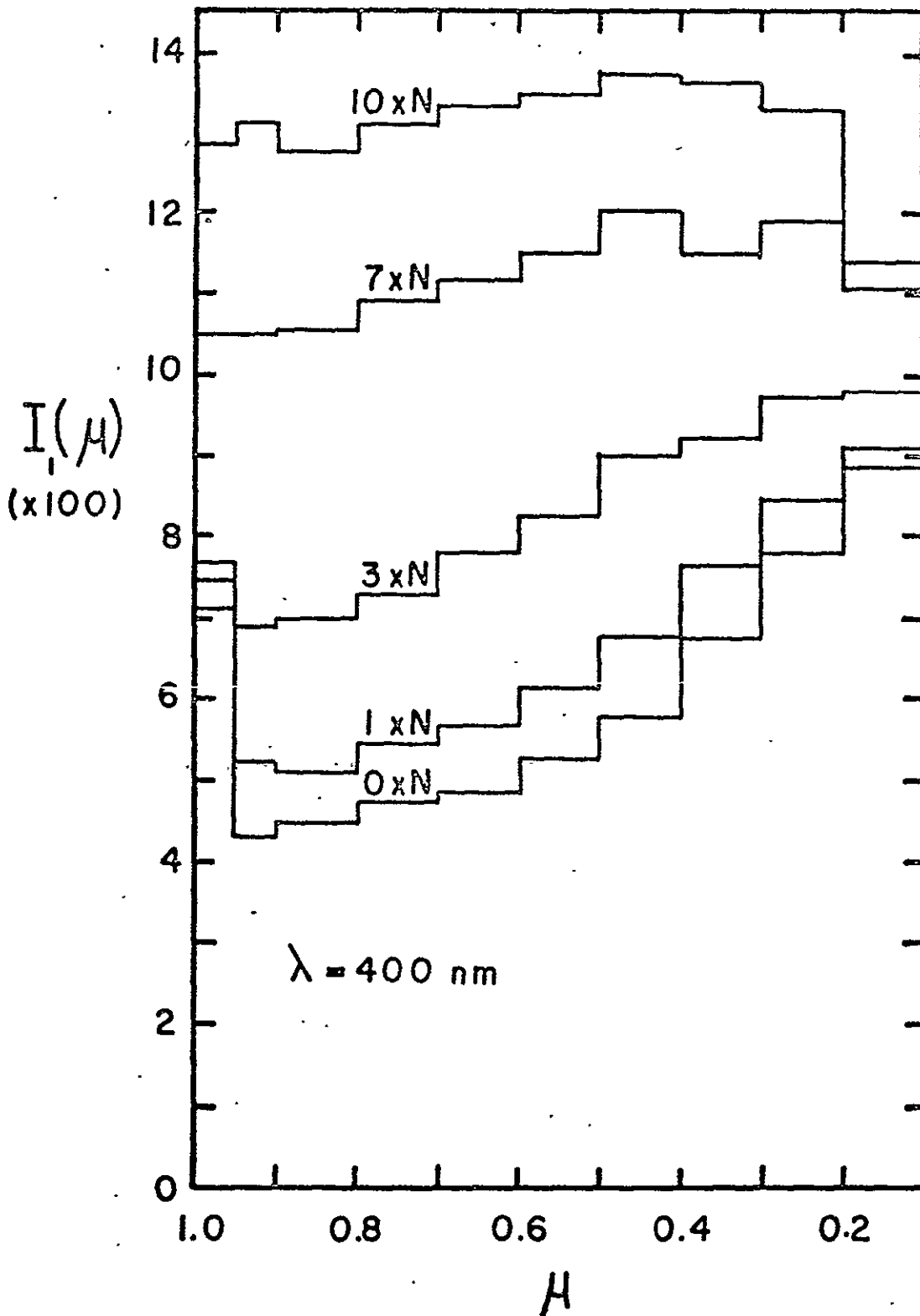*Figure 4.5* $I_1(\mu)$ *as a function of* μ *for various aerosol concentrations; wavelength of calculations is 400 nanometers.*
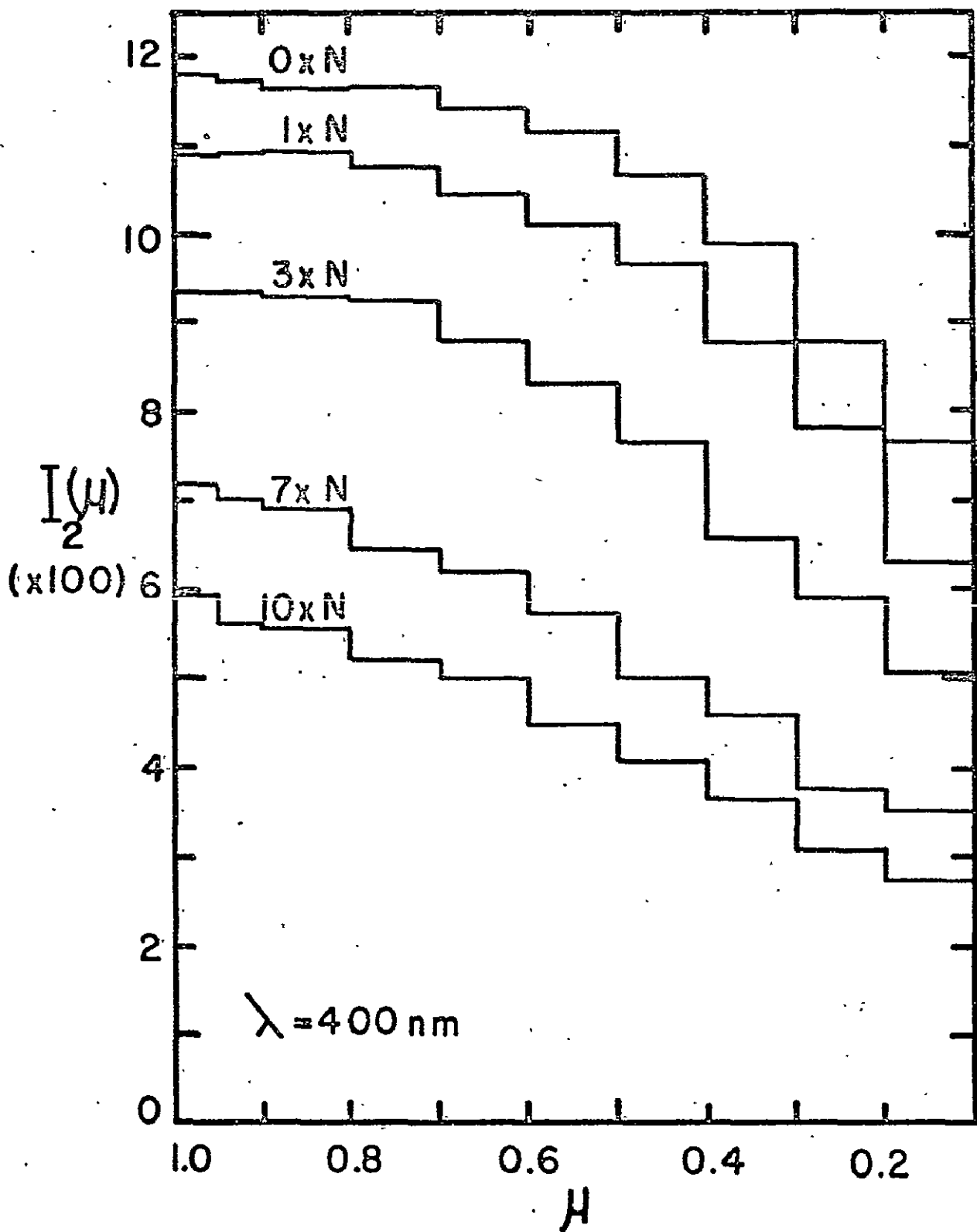
Figure 4.6 $I_2(\mu)$ *as a function of* μ *for various aerosol concentrations; wavelength of calculations is 400 nanometers.*

$$\frac{\partial I(\mu)}{\partial R} \cong I_2(\mu) \, .$$

Figure 4.6 shows that $\partial I/\partial R$ is not an extremely strong function of the aerosol concentration for concentrations up to three times normal, and viewing angles up to 35° from nadir. This suggests that horizontal gradients in R can be estimated without knowing the aerosol optical thickness with great accuracy.

Using equation 4.5 to relate changes in radiance($\Delta I(\mu)$) to changes in R(ΔR), i.e.

$$I(\mu) = [\partial I(\mu)/\partial R]\Delta R \cong I_2(\mu)\,\Delta R. \tag{4.8}$$

Equation 4.8a enables a determination of minimum radiance change the sensor must be able to detect for a given ΔR. For example, suppose that observing at $\mu = 0.85$ it is desired to detect a 5% change in R for clear ocean water at 400 nm ($R \approx .1$) through an atmosphere with 3 times the normal aerosol concentration. Figure 4.6 shows that $I_2(0.85)$ is about 0.11 and noting that the extra terrestrial flux 400nm is about 140 W cm^{-2} nm^{-1}, we find from equation 4.6 that $\Delta I(0.85)$ is 0.077 $Wcm^{-2}nm^{-1}sr^{-}$ In a similar way radiance changes can be related to ΔR for a nadir-viewing sensor and any solar zenith angle. As mentioned previously from the reciprocity principle,

$$I_{nadir} = I(\mu_0)\,\mu_0$$

where $\mu_0 = \cos\theta_0$, θ_0 is the solar zenith angle and $I(\mu_0)$ is the radiance at the top of the atmosphere seen by a sensor viewing at θ_0 when the sun is at the zenith. Following through with the same arguments that led to equation 4.8a it is found that

$$\Delta I_{nadir} = \mu_0[\partial I(\mu_0)/\partial R]\,R \cong \mu_0 I_2(\mu_0)\Delta R. \tag{4.8b}$$

Clearly, for a given ΔR, ΔI_{nadir} decreases substantially with increasing solar zenith angle due to the presence of the μ_0 factor in equation 4.8b. For example, with a 3 times normal aerosol concentration, a nadir viewing sensor would have to have about 2.5 times more sensitivity at $\theta_0 = 60°$ as compared to $\theta_0 \approx 0$ to detect the same R.

The above examples indicate how the theory (AS1) can be used in the design of a satellite sensor system for estimating some ocean property such as the concentration of suspended sediments or organic material. Specifically, one must first determine the effect of the property to be investigated on R, then based on the sensitivity desired, find ΔR, and finally, use equation 4.8a or b to find the minimum radiance change the sensor must be capable of detecting. If the sensor has a limited dynamic range, then equation 4.5 can be used with equations 4.8 a or b to aid in the sensor performance design trade-offs. [Unfortunately at this time, relationships between $R(\lambda)$ and sea water constituents are not well established.]
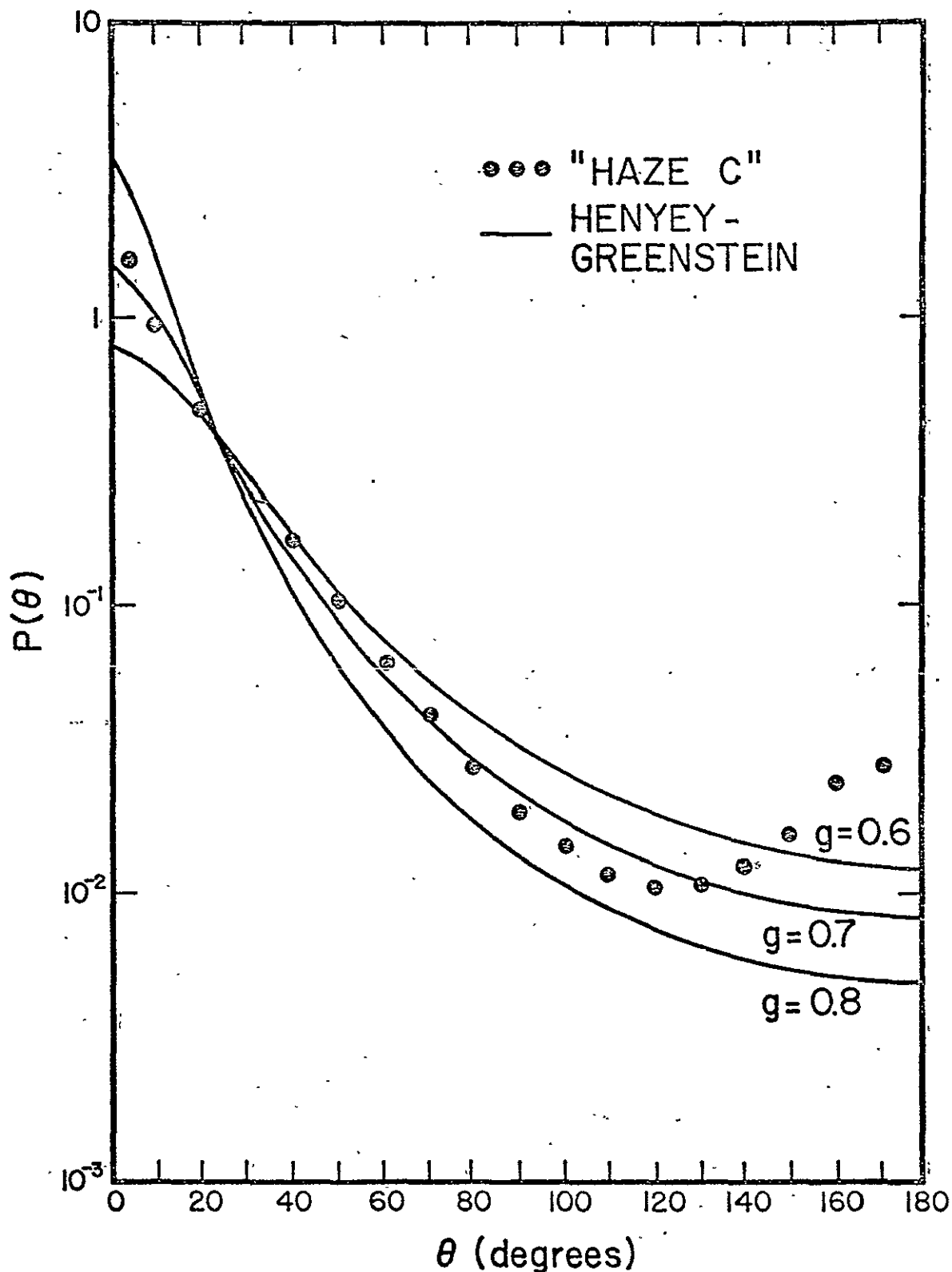
Figure 4.7 Comparison between the "haze C" and various Henyey-Greenstein
phase functions characterized by asymmetry parameters 0.6, 0.7, and
0.8, as a function of scattering angle (θ).

Considering the fact that we have only used the "haze C" aerosol phase function (which is clearly only approximately characteristic of the actual aerosol scattering) it is natural to inquire how strongly the computations of $I_1(\mu)$ and $I_2(\mu)$ presented in Fig. 4.5 and 4.6 depend on the shape of the aerosol phase function. To effect a qualitative understanding of the influence of the aerosol phase function, computations of I_1 and I_2 have been carried out using the well known Henyey-Greenstein[1](HG) phase function

$$P_{HG}(\theta) = \frac{(1-g^2)/4\pi}{(1+g^2-2g\cos\theta)^{3/2}}$$

where the asymmetry parameter g is defined according to

$$g = 2\pi\int_0^\pi P(\theta)\cos\theta\sin\theta\,d\theta,$$

and θ is the scattering angle. Since g for the "haze C" phase function is 0.690, computations have been made with $P_{HG}(\theta)$ for g values of 0.6, 0.7, and 0.8. Figure 4.7 compares these $P_{HG}(\theta)$'s with the "haze C" phase function. The HG phase function for g = 0.7 clearly fits the "haze C" phase function quite well in the range $5° \leq \theta \leq 140°$; however, as is well known, the HG formula is incapable of reproducing phase functions computed from Mie theory in the extreme forward and backward directions. The HG phase functions with asymmetry parameter 0.6 and 0.8 are seen to be substantially different from the "haze C" distribution at nearly all scattering angles. On the basis of Fig. 4.7 it should be expected that I_1 and I_2 computed with $P_{HG}(\theta)$ will be in close agreement with the "haze C" computations only for g close to 0.7. Figures 4.8 and 4.9, which compare the results of computations of I_1 and I_2 respectively for $P_{HG}(\theta)$ with g = 0.6, 0.7, 0.8 (step like lines) and the "haze C" phase function (solid circles) for the normal aerosol concentration, show that this is indeed the case. It is seen that except for apparent statistical fluctuations, the HG phase function for g = 0.7 yields values of I_1 and I_2 in good agreement with the "haze C" computations. This suggests that the detailed structure of the phase function is not of primary importance in determining I_1 and I_2, and it may be sufficient for remote sensing purposes to parameterize the phase function by g.

To get a feeling for the importance of variations in the phase function in the remote sensing of ocean color, consider the effect of changing the aerosol phase function from an HG with g = 0.6 to g = 0.8 over an ocean with R = 0.1. From Fig. 4.8 and 4.9 it is found that the normalized radiance at $\mu = 0.85$ (the assumed observation angle) decreases by 4.9×10^3, this decrease in radiance would be interpreted under the assumption of no atmospheric change as a decrease in R from 0.10 to 0.056. This clearly indicates then that variations in the aerosol phase function in the horizontal direction could be erroneously interpreted as horizontal variations in the optical properties of the ocean. It is however probably unlikely that except in extreme cases, the clear atmosphere oceanic aerosol phase function will exhibit variations as large as considered in this example. Assuming that the aerosol concentration of the atmosphere can be determined, the uncertainty in the aerosol

Figure 4.8 Comparison between $I_1(\mu)$ computed for the "haze C" and Henyey-Greenstein phase functions for an atmosphere with a normal aerosol concentration, as a function of cosine $\theta(\mu)$; wavelength of calculations is 400 nanometers.
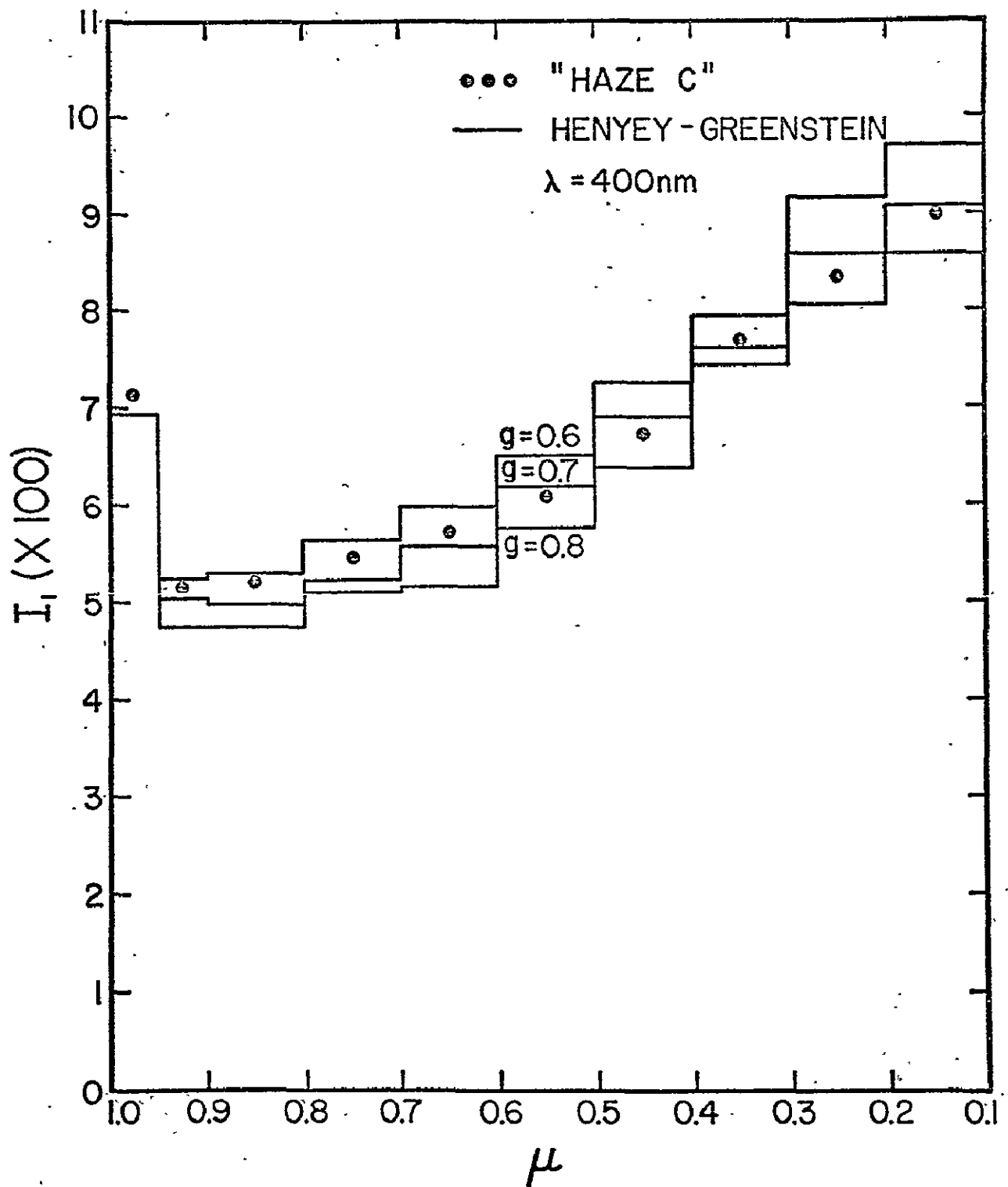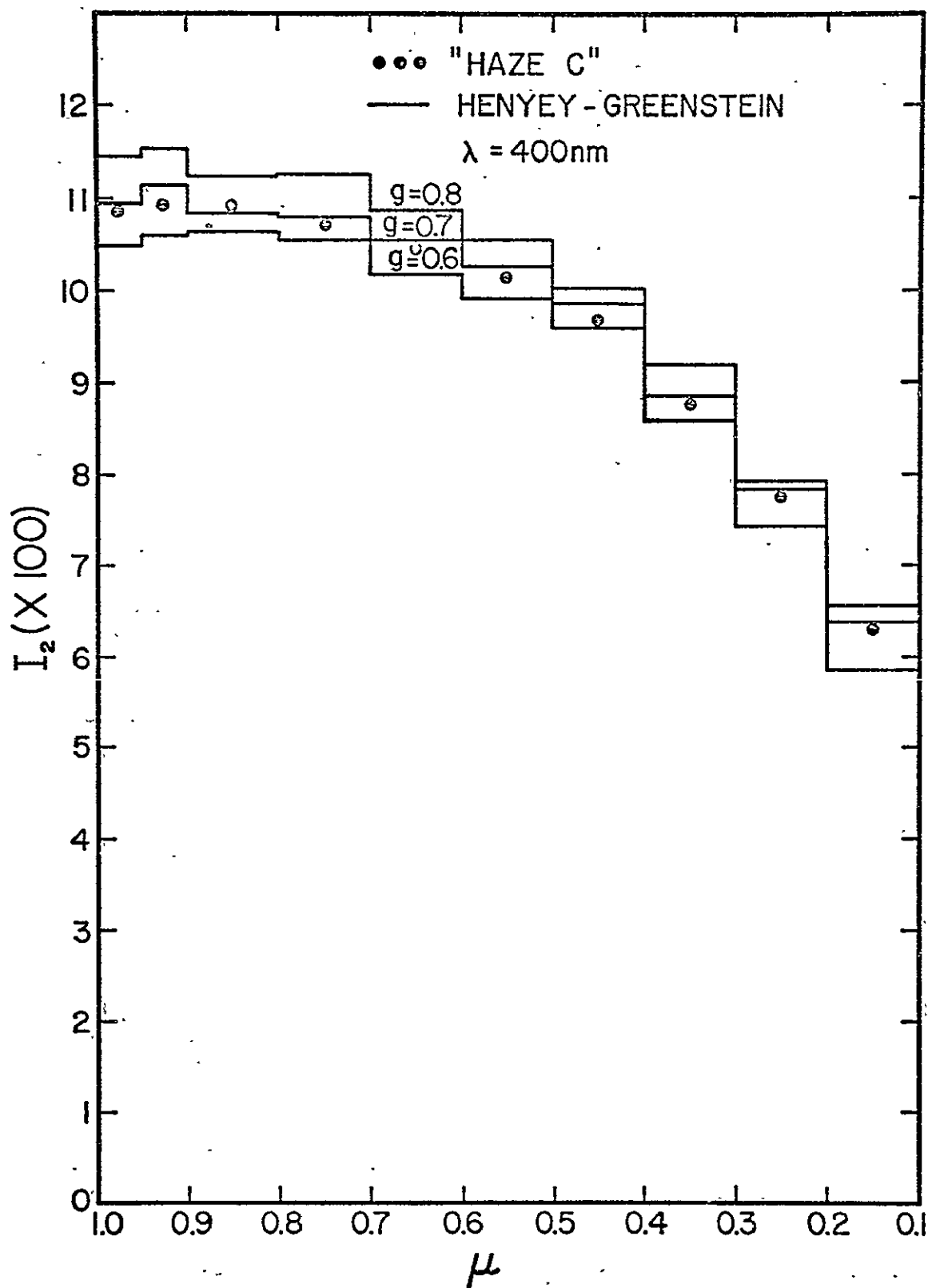
Figure 4.9   Comparison between $I_2(\mu)$ computed for the "haze C" and Henyey-Greenstein phase functions for an atmosphere with a normal aerosol concentration, as a function of cosine $\theta(\mu)$; wavelength of calculations is 400 nanometers.

phase function will still of course provide a limit to the accuracy with which the ocean color-spectrum can be retrieved from satellite radiance measurements.

In summary then, the theory (AS1) leads to the natural definition of $R(\lambda)$ [$R(0,-)$ as a function of wavelength] as the "ocean color spectrum". The determination of subsurface oceanic properties from space can thus be divided into two problems: 1) the determination of $R(\lambda)$ from satellite radiance measurements, and 2) the establishment of relationships between $R(\lambda)$ and the desired ocean properties. Since the method of computation conveniently separates the radiance into a component that interacts with the ocean (I_2) and a component due to reflection from the atmosphere and sea surface (I_1), it is easy to relate changes in radiance to changes $R(\lambda)$. It is found that for viewing angles up to 35° from nadir, I_2 is a relatively weak function of the aerosol concentration for concentrations up to 3 times normal. This suggests that spatial gradients of $R(\lambda)$ can be determined with only a rough estimate of the aerosol concentration. It is further found that variations in the aerosol phase function can strongly influence the interpretation of the radiance at the satellite. Clearly then, it is vital to understand the magnitude of aerosol phase function variations.

4.2.2 Technique for Atmospheric Correction

As discussed in section 4.2.1 it is necessary to know the aerosol concentration in order to recover the "ocean color spectrum" $R(\lambda)$ from the nadir radiance spectrum observed at the satellite. In this section a method based on Curran's suggestion of using the near infrared radiance to determine the concentration is developed and applied to the S-191 data.

The method involves finding a band of wavelengths in the near infrared for which the absorption by ozone and water vapor is negligible. Since the Rayleigh scattering by air is very small in the near infrared the greatest contributor to the optical thickness at the wavelength in question is the aerosol. It is found that at 780 nm ozone and water vapor do not absorb significantly, and the Rayleigh scattering only contributes about 0.023 to the total optical thickness of the atmosphere, implying that aerosols play the dominant role in the radiative transfer here with the normal aerosol concentration yielding an optical thickness of about 0.2. Also since $R(0,-)$ for wavelengths greater than about 700 nm is essentially zero, the upward radiance at the top of the atmosphere at 780 nm simply becomes

$$\frac{I(\mu)}{F_o} = I_1(\mu)$$

where F_o is the solar irradiance (mW cm^{-2} μm^{-1}), at the top of the atmosphere and is taken from Kondrat'ev. (1973). Using the the reciprocity principle, for nadir viewing and any solar zenith angle (θ_o), I_{nadir} can be written

$$I_{nadir} = \mu_o F I_1(\mu_o).$$

$I_1(\mu)$ and $I_2(\mu)$ have been computed for aerosol concentrations 0xN,1xN

-42-

2xN and 3xN at 400 nm, 500 nm, 600 nm and 780 nm and the results for the
0xN and 1xN computations are presented in Appendix C. Using $I_1(\mu)$
for 780 nm and noting that the S-191 nadir radiance was recorded with $\theta_a \cong$
40° the upward radiance at the top of the atmosphere for nadir viewing is
found to be 0.323 and 0.938 m $W cm^{-2}$ $sr^{-1} \mu m^{-1}$ for aerosol concentrations of
0xN and 1xN respectively. Using the S-191 radiances at 780 nm for
the nadir viewing spectra taken on Jan. 8, 1975 at 16:30:45.75 GMT
(spectrum A) and 16:30:52.2 GMT (spectrum B) which respectively were
0.64 and 0.72 m$W cm^{-2}$ $sr^{-1} \mu m^{-1}$, it is found that the theory suggests the
aerosol concentration was 0.51 xN for spectrum A and 0.64 xN for spectrum B.
In order to compute $R(\lambda)$ from the S-191 data the assumption is made that
the variation of the aerosol extinction coefficient with wavelength is
exactly as given by Elterman.

4.2.3 Recovery of $R(\lambda)$ from the S-191 data

As mentioned above, in order to recover $R(\lambda)$ from the S-191 data
it is necessary to assume that the variation of the aerosol extinction
coefficient with wavelength is identical to that given by Elterman. Also,
since $I_1(\mu)$ and $I_2(\mu)$ at 780 nm were derived using the "haze C" phase
function for the aerosols, the assumption this phase function is correct
is implicitly being made. With these assumptions the nadir radiance
at the top of the atmosphere has been computed at 400, 500, 600 and 780
nm for aerosol concentration 0xN and 1xN assuming that $R(\lambda)$ is zero, and
these are presented in Table 4.3 along with the radiances from spectra A
and B.

Since the aerosol concentration is known to be between 0xN and 1xN
it appears that the S-191 data at 400 nm is in error. It is virtually
impossible for the nadir radiance to be less than that for a 0xN atmos-
phere. (It should be noted that the discrepancy here is not small,
i.e. the S-191 radiances at 400 nm appear to be too small by more than
a factor of 2.) The radiances at the other wavelengths listed in
Table 4.3 seem to be reasonable and these will be used to estimate
$R(\lambda)$ using equation 4.7. The results of this are shown in Table 4.4.

It is seen that $R(\lambda)$ is negative except in the spectral region 500-
550 nm where the values shown compare well with the Tyler and Smith Gulf
Stream data for R(0,-). As discussed above, the 400 nm data is appar-
ently in error, however the data at other wavelengths appear realistic,
so the negative R(0,-) values are probably due to the assumptions
that the "hazeC" phase function characterizes the aerosol, and that
the spectral variation of the aerosol scattering coefficient is correctly
described by Elterman's data. It should be clear that considerably more
experimental work is required in order to test the ability of the theory
discussed in 4.2.1 to accurately find $R(\lambda)$ from the satellite radiance.

<div align="center">Table 4.3</div>

Wavelength (nm)	F_O $\text{mW cm}^{-2}\mu\text{m}^{-1}$	I_{nadir} (R=0) $\text{mw cm}^{-2}\mu\text{m sr}^{-1}$			
		0xN	1xN	Spect A	Spect B
400	157	5.61	6.58	2.30	2.50
500	201	2.93	4.10	4.13	4.39
600	184	1.25	2.13	1.55	1.67
780	125	0.323	0.938	0.64	0.72

<div align="center">Table 4.4</div>

Wavelength (nm)	R(0,-)	
	Spectrum A	Spectrum B
400	-0.274	-0.268
450	-0.0242	-0.0235
500	0.0318	0.0370
550	0.0295	0.0303
600	-0.00715	-0.00547
780	0	0

5. MULTISPECTRAL SCANNER EXPERIMENT

SKYLAB's multispectral scanner was a unique design that had 13 spectral channels of data spread over the visible and infrared bands. The system used a conical scan which had the advantage of keeping the atmospheric path length the same at all times. The visible region of the spectrum (0.4 - 0.75μm) was divided into 6 channels, each about 0.05 μm wide. Two reflected infrared (0.75 - 1.0 μ m) channels and one in the emitted infrared (10.2 - 12.5 μm) were also provided. The channels useful to oceanography, which were examined in this experiment, are summarized in table 5.1.

LANDSAT-1 has been shown to have several useful applications of visible region imagery to marine science (Maul, 1974). The much finer spectral resolution of the S-192 provided an opportunity to expand those results to ocean current boundary determination and to test if the lower wavelength (0.5 μm) intervals were useful through the intervening atmosphere.

5.1 S-192 Data

S-192 data were collected from 16:29:22 GMT (over the open sea just north of the Cuban coastline) to 16:31:04 GMT (over the mainland Florida coast north of Florida Bay). All channels listed in table 5.2 were carefully examined in the analog format provided by NASA to the principle investigator. The data in the images were compared with the S-190A and S-190 B photographs to see if what is interpreted in section 3.2 as the anticyclonic edge of the current could be detected. This feature was not observable in the standard data product.

The cyclonic edge of the stream appears to be obscured by clouds. This is often a useful means of locating the edge of the current but unfortunately made the objective of directly sensing the edge an impossibility.

An unexpected opportunity to evaluate the S-192 however, is evident in the photographic detection (section 3) of a mass of water from Florida Bay flowing south into the Straits of Florida just west of Key West. This water is observed to be milky in appearance and somewhat greener in color. No ocean surface spectra were observed inside or outside of the plume of Florida Bay water, although it could have been easily accomplished if the SKYLAB crew had observed the feature and radioed the observation,so tha the ship knew of its presence. Upwelling spectral irradiance reported by Maul and Gordon (1975) probably describe the essential features of the plume and water in the straits.

An intensive effort was made by Norris (NASA-JSC), Johnson (Lockheed-JSC), and Maul (NOAA-AOML) to extract the two features discussed above using the computer enhancement facilities at NASA-JSC. After approximately

TABLE 5.1

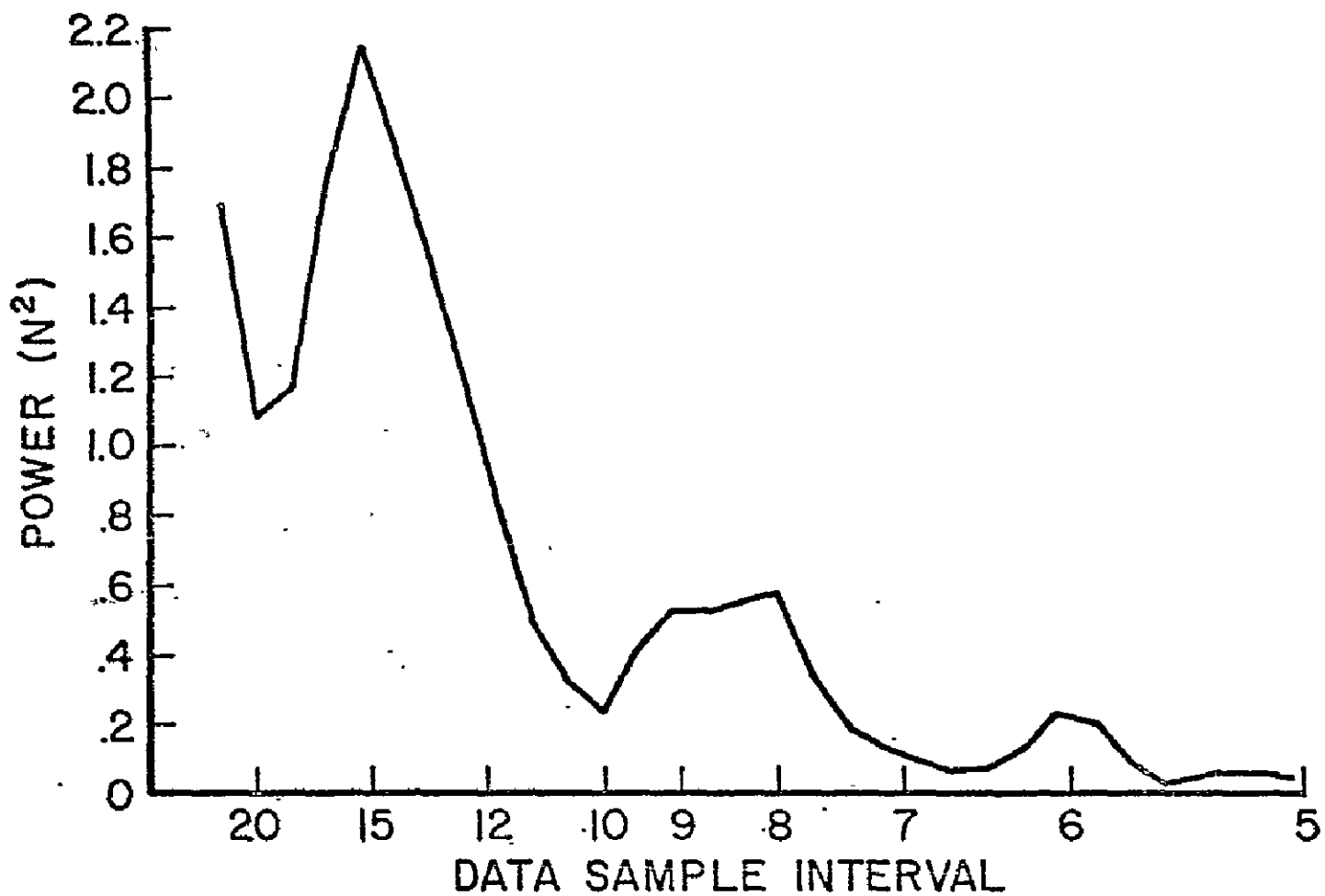| BAND	DESCRIPTION	RANGE (µm)
1	Violet	0.41 - 0.46
2	Violet-Blue	0.46 - 0.51
3	Blue-Green	0.52 - 0.56
4	Green-Yellow	0.56 - 0.61
5	Orange-Red	0.62 - 0.67
6	Red	0.68 - 0.76
7	Reflected Infrared	0.78 - 0.88
8	Reflected Infrared	0.98 - 1.03
13	Thermal Infrared	10.2 - 12.5

*Figure 5.1 Power spectrum of the radiance in the unfiltered S-192
conical format. Significant noise is noted every .5, 10-8, and
6 data points.*

10 hours of machine time on both conical and line straightened data, the feature described as the anticyclonic edge could not be identified, although it is clearly brought out in the photographic enhancements (see Fig. 3. 2). Further effort to bring out the anticyclonic edge was judged to be unwarranted and attention was turned to the plume feature which is visible in Fig. 3. 3, and which preliminary enhancement at the NASA-JSC facility showed to be a useful area in which to work.

Prior to developing a general computer enhancement technique, the data were examined for periodic features in a TUKEY spectrum. Figure 5.1 is a spectrum of data specially provided for this experiment that was to be high pass filtered only; the calibration of the S-192 is considered a high pass filter. Significant periods at about 15 data sample intervals is noted in these conical data as has been reported (Schell, Philco-JSC, personal communication 1975.) The line straightened data (see Fig. 5.2) have been band pass filtered to remove this 15 data sample periodicity . The wavy patterns near the edge of clouds is the result of filter ringing.

5.2 Computer Enhancement

Computer enhancement of S-192 data was an objective of the experiment. The technique described below is a step toward automatic detection of clouds in multispectral data. The goal is to use a near infrared channel (channel 8 in this case) to specify where cloud free areas are for analysis of sea surface temperature, or ocean color.

Channel 8 ($0.98-1.03 \mu$ m) is selected as the cloud discrimination channel because there is a maximum in the atmospheric transmissivity at this wavelength, and a maximum in the absorption coefficient of water. The high absorption coefficient of water at 1μ m causes the ocean surface to have a very low radiance when compared with land or clouds. Thus there should be two modes in the frequency distribution of radiance: one mode for the clear ocean and another mode for land and/or clouds. An example of such a bimodal distribution is given by the histogram in Fig. 5.4.

In this figure, the low ocean radiances are clustered at the mode centered at $N = 0.2$ μW cm^{-2} sr^{-1} . The other mode, centered at $N = 5.7$ μWcm^{-2} sr^{-1} is a contribution of the clouds (there is no land in this example). If these modes can be identified and separated, a statistical identification of cloud-free ocean pixels can be made.

Cox and Munk (1954) observed that the radiance reflected from the ocean is essentially Gaussian in character. The problem then is to fit a curve of the form

$$y = \frac{ni}{\sigma \sqrt{2\pi}} \exp [-(N - N)^2/2\sigma^2] \qquad (5.1)$$

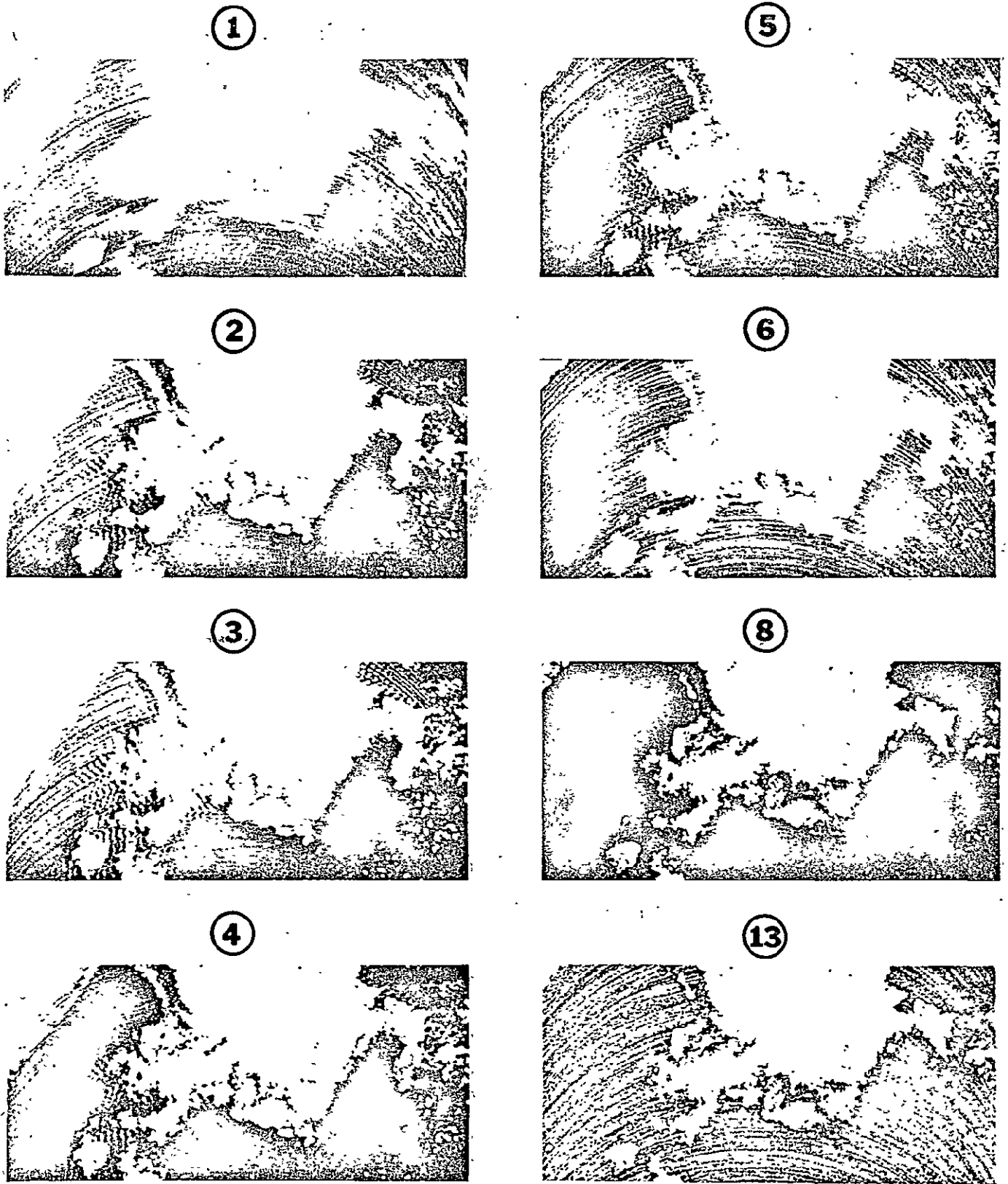Figure 5.2 S-192 line straightened, filtered, scanner data over the Straits
of Florida near the western Florida Keys. The S-192 channel number is at
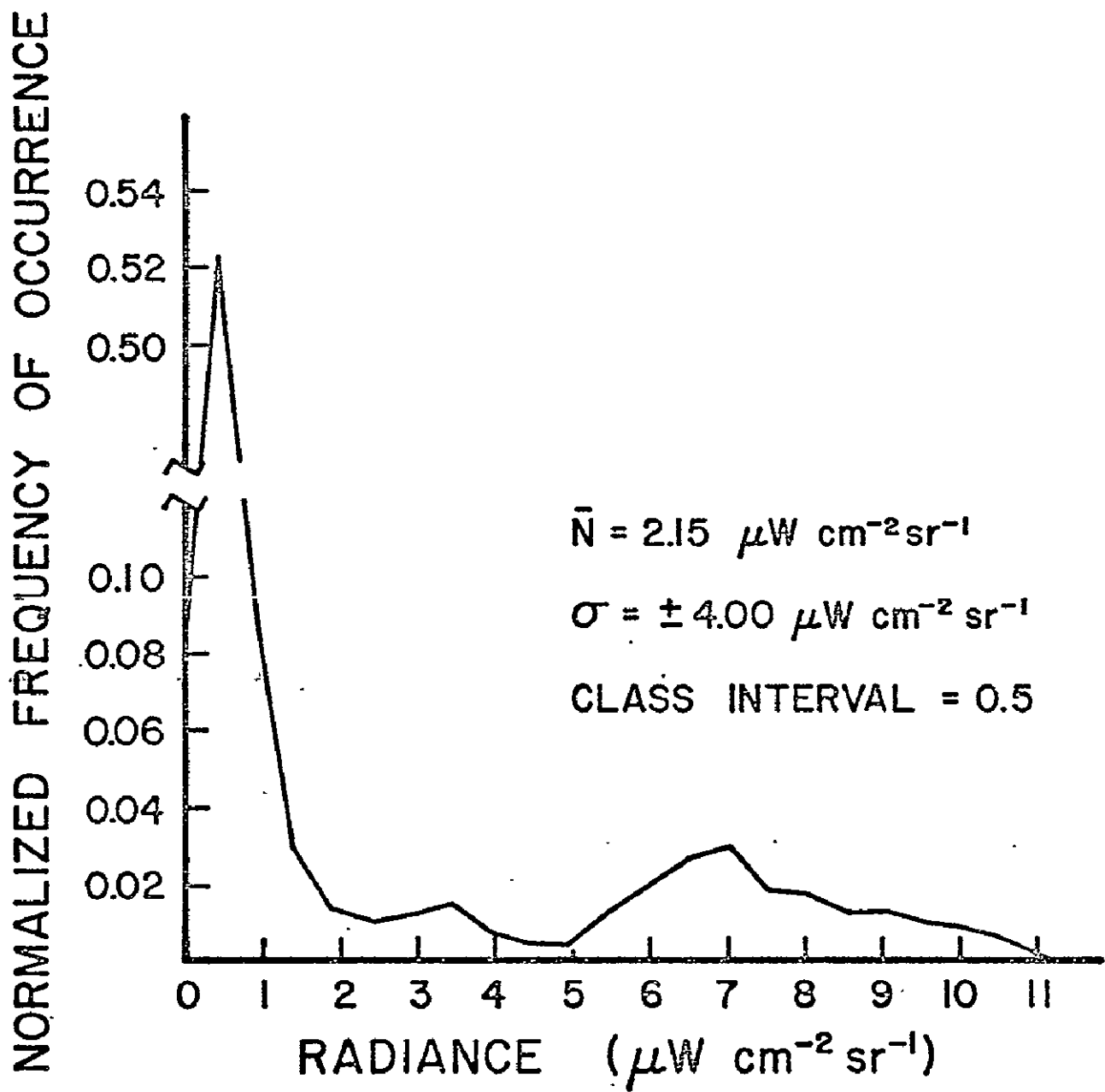the top of each appropriate panel.

*Figure 5.3 Histogram (normalized to unity) of the radiance in channel 8
over the same area as figure 5.2 the primary peak at the left is clear
ocean; the broad peak centered at 7 μm cm^{-2}sr^{-1}is due to clouds and land.*

to the data at the lower valued mode. In this equation, the normal frequency curve (y) is a function of the total number of observations (n), the class interval (i), and the standard deviation (σ); the overbar on the dependent variable (N) denotes ensemble average. Fitting equation 5.1 to the data is done in an iteration scheme that uses the lower valued mode as a first estimate of $\bar{N}$ (only the values $N \pm 2\sigma$ from the original ensemble are used in this first iteration; this eliminates much of the cloud contaminated data). After the first fit using a prescribed $\bar{N}$, the scheme is to iterate the data using only $+2\sigma$ of each new fit. When σ (or $\bar{N}$) changes less than 0.1% between iterations, the fit is considered acceptable and the cloud free pixels are defined as those between $0 < y < +3$. This guarantees that 99% of the values around the lower mode are accepted and included in the ocean data. Experience with this algorithm suggests that only 5 or 6 iterations are usually necessary for the scheme to converge.

In Fig. 5.4, the data from the left hand portion of Fig. 5.3 are plotted along with the fitted frequency distribution given by equation 5.1. This fit required 5 iterations. Cloud-free data are conservatively identified as all those whole $N \leq 0..5 \mu W\ cm^{2}\ sr^{1}$ ($\bar{N} + 3\sigma$). Data from any other channel can now be statistically examined on a pixel by pixel comparison with channel 8; only "cloud-free" values go into the statistics.

Cloud free data from any other channel are analyzed for their mean and standard deviation. These calculations automatically provide the limits over which the ocean data are to be stretched. Following the technique suggested by Maul, Charnell, and Qualset (1974), the formulation used by Maul (1975) is used here. The stretch variable (ζ) for a negative image is defined by:

$$\zeta = 0 \ \text{for}\ N \geq \bar{N} + \kappa \sigma$$

$$\zeta = \frac{M\ [(\bar{N} + \kappa \sigma) - N]}{2\kappa\sigma} \quad \text{for}\ (\bar{N} - \kappa\sigma) \leq N \leq (\bar{N} + \kappa\sigma)$$

$$\zeta = M \ \text{for}\ N < \bar{N} - \kappa\sigma.$$

In this formulation M is the maximum value allowed by the Digital-to-analog (D/A) output device, $\bar{N}$ is the mean radiance of the cloud free data, and is a constant. Considering N a continuous variable, setting $\kappa = 2$ would stretch 95% of the cloud free data over the full range of the photographic enhancement device.

The technique described above allows an objective specification of both the range of settings for an optimum enhancement of an ocean scene, and a statement of the radiance range required of an ocean color sensor under these conditions. In Fig. 5.6, the data from the sediment plume flowing through the Florida Keys are presented for channels 1-6,8, and 13. These data are not line-straightened and they are only high pass filtered. While the data are distorted geographically, they represent the best radiometric information from the S-192.
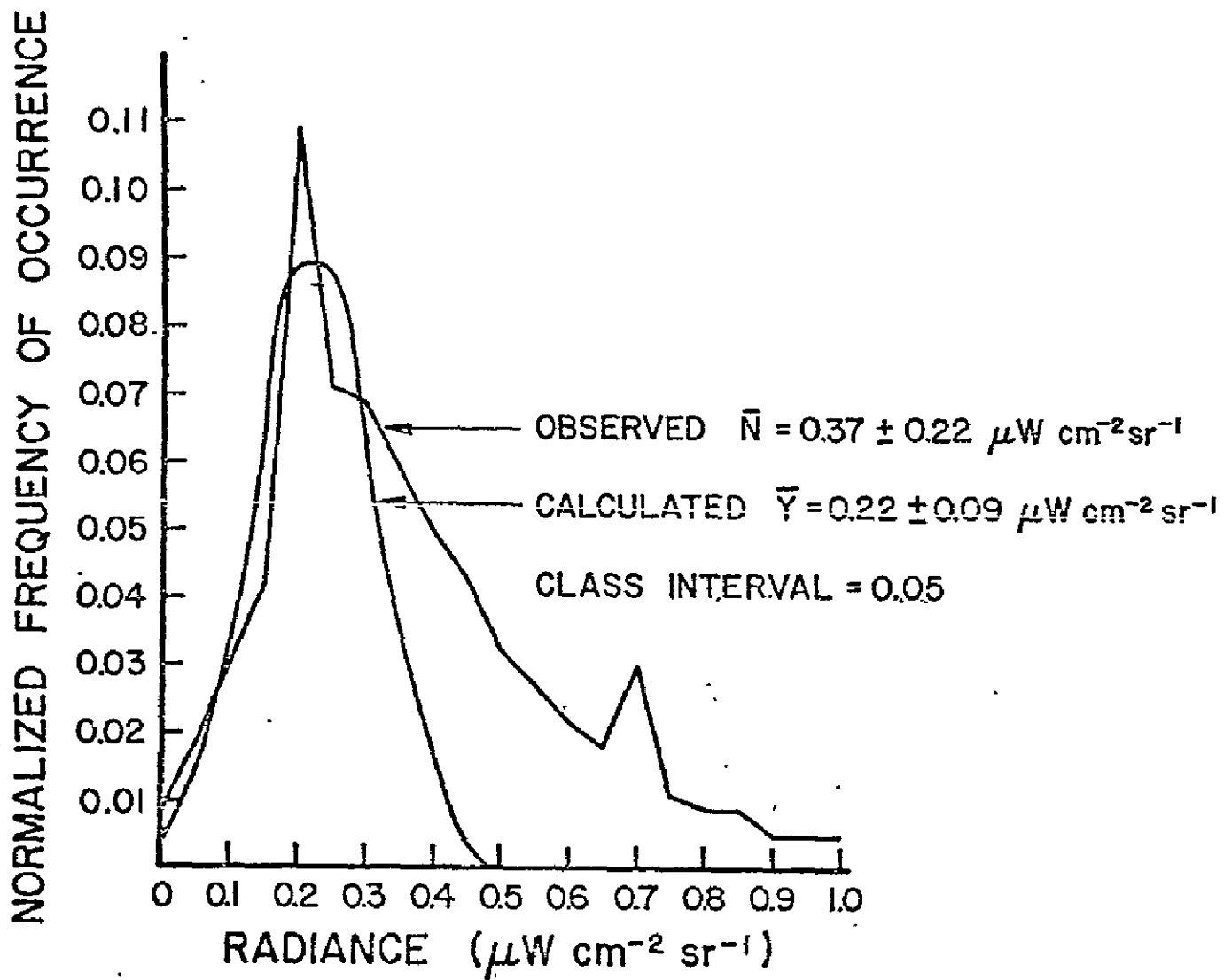
Figure 5.4   Expansion of low radiance portion of the histogram in Figure 5.3. The smooth curve's the fitted Gausian approximation to the observed radiance distribution.
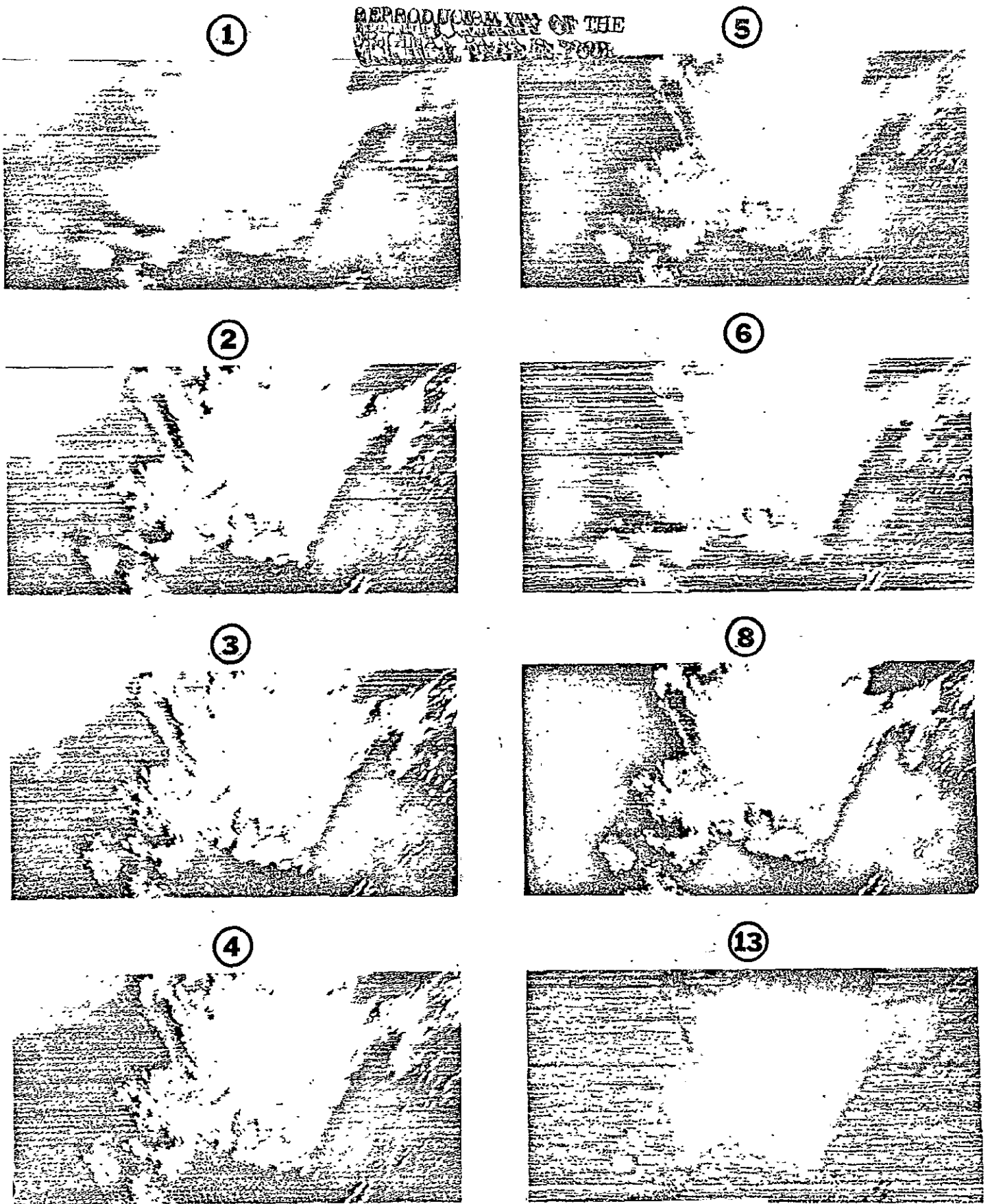
Figure 5.5   Conical S-192 imagery of the same area as shown in figure 5.2.
Channel 8 in this figure is a binary mask with clear ocean black, and
clouds, land, and other unwanted pixels white.

TABLE 5.2

Channel	Mean ± σ	Oceanic Radiance Range $mW\ cm^{-2}sr^{-1}\mu m^{-1}$
1	3.56 ± 0.45	2.21-4.91
2	4.71 ± 0.97	1.80-7.62
3	4.07 ± 1.33	0.08-8.06
4	2.83 ± 1.46	0.00-7.21
5	1.73 ± 0.92	0.00-4.49
6	0.93 ± 0.43	0.00-2.22
7	0.57 ± 0.29	0.00-1.46
8	0.37 ± 0.22	0.00-1.03
13	0.80 ± 0.03	0.71-0.89

5.3 Discussion

Without actual spectra as surface truth it is not possible to adequately interpret the scanner data in the vicinity of the plume. Other spectral data (see Section 4.2 and Maul, 1975) suggest that there should be a detectable difference in the data from channels 1 through 5. Little information, let alone information difference, is contained in channel 1 (see again Figs. 5.2 & 5.6). These findings are in agreement with Hovis (NASA-GSFC, personal communication, 1975) who found that little or no information is detectable through the atmosphere for wavelengths much less than 0.45 μm. The Rayleigh scattering at shorter wavelengths is so intense that multispectral scanners such as the S-192 or the coastal zone color scanner destined for NIMBUS-G should not have a violet (0.41 - 0.46μm) channel. This means that the wavelengths which contain much of the oceanographic information are of little value at orbital altitudes.

Analysis of the conical data used in Fig. 5.6 allows a specification of the radiance range encountered. Since an ocean color sensor should be allowed to saturate over land or clouds, the range appears narrow. The range is based on $\pm 3\sigma$, which describes 99% of the data encountered herein. Saturation at higher signal levels is recommended in order to expand the quantization commensurate with an acceptable data flow rate. Table 5.2 lists the radiance ranges.

This range of values applies only to this data set, which represents low latitude, winter conditions. A similar analysis of S-192 data from other areas of the oceans and at other times would lead to an objective statement of the radiance range specification for an oceanic color sensor. Note that the lower value on the shorter wavelength channels is non-zero this reflects the radiance of the atmosphere only.

Neither the line-straightened (Fig. 5.2) nor the conical (Fig. 5.5) imagery was capable of detecting any ocen thermal variations. The thermal data (channel 13) were processed in both negative and positive format in an attempt to show some of the 2°C range recorded in the surface observations (Fig. 2.1). In comparing the data, note that the area covered is not identical due to geographical distortion in the line-straightened processing.

The actual mask generated from using equations 5.1 is illustrated in the channel 8 data in Fig. 5.2 . Here the values 0 or 3 are assigned for contaminated or ocean (respectively) radiances. The channel 8 data in Fig. 5.5 were simply stretched over the $\pm 2\sigma$ range by equations 5.2. A significant error in the automatic stretch units of other channels would occur if the extra step of 0 or 1 assignment were not made, because of the exclusion of some ocean radiances. Note also that the effect of filter ringing is eliminated in the Fig. 5.2 masking; this can also lead to wrong stretch limits if care is not exercised in application of the technique. Filtering should always be done after the data are masked.

The conical scan technique is an unusual approach to multispectral scanning. Data quality of the S-192 is judged to be poorer than experience with the LANDSAT MSS which uses a linear scan. If the poorer S-192 data is inherent in the design of all conical scanners then it cannot be recommended for the NIMBUS-G; coastal zone color scanner. If this is not the case there is no reason based on this investigation to not consider such a future design.

6. SUMMARY

The objectives of this experiment were to obtain simultaneous ship, aircraft, and spacecraft data across the Gulf Stream in the Straits of Florida in order to evaluate several techniques for remote sensing of this ocean current. Calibration of the S-191 infrared detectors was not known; this precluded comparing the atmospheric transmission models, which was an objective. Detection of the current with the photographs was possible but the S-192 scanner was not useful in this respect because the gain settings were not adequate for ocean radiances. A technique to determine atmospheric corrections for visible radiometers based on theoretical considerations was shown to be promising. Details of those results are enumerated below:

1. Observation and data reduction techniques for surface truth vessels include measurement of ocean color spectra from 3 meters above the surface. Objective filtering techniques were developed to remove periodic specular return caused by wave facets. (section 2.3)

2. The limited photographic (S-190) data set in this experiment provides a baseline against which satellite photos of more biologically productive waters may be compared. Intercomparisons with aircraft derived photography may be more difficult. This problem was not resolved in this experiment because of unforseen variation in the exposure level of these photos.(section 3.)

Non-uniformity in the satellite space-derived photography is probably mostly due to the effects of variable lens transmission. It is recommended that the production of multiple generation photos ("dupes") be documented in a manner similar to that of the original films. This should include some documentation on the printer light variation across the platen, suspected to be a major source of the variability measured in the dupes used in this experiment. (section3.2)

3. The data acquisition camera on SKYLAB was not turned on during the experiment; this made any quantitative comparisons with spectra impossible. There should be a positive interlock on all future missions to prevent a reoccurrence. Spectra were not obtained across the Gulf Stream front because a) no data just prior to the mission were obtained, and b) no direct communication link from the ship to the spacecraft could be set up. Future experiments must include a mechanism to communicate to surface truth investigators the position of variable features such as

ocean currents. (section 4.0)

,4. Unfortunately the S-191 visible near-IR data could not be used to study the observability of oceanic fronts from satellite altitudes because the Gulf Stream front was missed. However, a theoretical method for recovering the "Ocean Color Spectrum" through the atmosphere was developed. This was used to try and retrieve the "ocean color spectrum" from the nadir-viewing S-191 data,with limited success. The results agreed well with measurements (Tyler and Smith, 1970) for wavelengths greater than 500 nm, but in the blue the S-191 radiance was substantially smaller than previous aircraft observations; and even a factor of 2 less than theoretical predictions for an aerosol free atmosphere. This is either due to a malfunction of the sensor in the blue or to the presence of a very strongly absorbing aerosol. Our present knowledge of the optical properties of marine aerosols does not appear to be sufficiently complete to effect a quantitative retrieval of "ocean color spectrum" from spacecraft data. Clearly further research on this problem is indicated. (Section 4.2)

5. Ocean features that were visible in photographs (section 3.2) were not visible in the S-192 multispectral scanner data due to the lack of radiance resolution. The range of radiances needed to adequately observe ocean features is presented in table 5.2. These data support the view that an ocean color multispectral sensor can do without a channel equivalent to channel 1 (0.41 - 0.46µ m) of the S-192, as no information on a very strong color boundary was contained in those data (section 5.3).

An objective S-192 cloud detection technique was developed that uses Gausian statistics to identify cloud-free areas in channel 8 (0.98 - 1.03 µm). Cloud-free pixels are then analyzed in other channels so that contrast stretching based on the same statistics is automatically accomplished (section 5.2).

7. ACKNOWLEDGEMENTS

8. REFERENCES

1. Anding, D. (1975): Final report to NASA-JSC on SKYLAB experiment, in press.

2. Anding, D. and R. Kauth (1970): Estimation of Sea surface temperature from space, Remote Sensing of Environ.,1(4), pp 217-220.

3. Anding, D. and Kauth, R. (1972): Reply to comment by G. Maul and M. Sidran, Remote Sensing of Environ., 2(3), pp. 171-173.

4. Baig, S.R. (1973): Spectral properties of Some Marine Phytoplankters, J. Soc. of Mot. Pict. & T.V. Engrs., 82, pp. 1007-1012.

5. Baig, S.R. and Atwell, B.H., (1975): Spectra of Phytoplankters in Aqueous Suspension, (in preparation)

6. Baig, S.R. and Yentsch, C.S., (1969): A Photographic Means of Obtaining Monochromatic Spectra of Marine Algae, Appl. Opt. 8(12), pp. 2566-2568.

7. Chandrasekhar, S. (1960): Radiative Transfer, Dover Press, N.Y., 393 pgs.

8. Curran, R. (1972): Ocean color determination through a scattering atmosphere., Appl. Opt., 11, pp. 1857-66.

9. Davis, P.A., and Viezee, W. (1964): A Model for Computing Infrared Transmission Through Atmospheric Water Vapor and Carbon Dioxide, J. Geophys. Res., 69, pp. 3785-3794.

10. Deirmendjian, D. (1964): Scattering and Polorization Properties of Water Clouds and Hazes in the Visible and Infrared, Appl. Opt., 3, pp. 187-96.

11. Duntley, S.Q., Austin, R.W. Wilson, W.H., Edgerton, S.F. and S.E. Moran,(1974): Ocean Color Analysis, Scripps Institution of Oceanography, San Diego, Calif., Ref. 74-10, 72 pgs.

12. Elterman, L., (1968): UV, Visible, and IR Attenuation for Altitudes to 50 km., 1968, Air Force Cambridge Research Laboratories Report AFCRL-68-0153.

13. Gordon, H.R. (1973): Sample Calculation of Diffuse Reflectance of the Ocean, Appl. Opt. 12, pp. 2803-4.

14. Gordon, H.R., and Brown, O.B., (1973): Irradiance Reflectivity of a Flat Ocean as a Function of its Optical Properties: Appl. Opt., 12, pp. 1549-51.

15. Gordon, H.R. and Brown, O.B., (1974): Influence of Bottom Depth and Albedo on the Diffuse Reflectance of a Flat Homogenous Ocean, Appl. Opt.,13, pp. 2153-59.

16. Gordon, H.R., and Brown, O.B., (1975): A Multiphase Monte Carlo Technique for Simulation of Radiative Transfer, J. Quant. Spectrosc. Radiat. Transfer, 15, pp. 419-22.

17. Gordon, H.R., Brown, O.B., and M.M. Jacobs, (1975): Computed Relation-ships Between Inherent and Apparent Optical Properties of a Flat Homogenous Ocean, Appl. Opt. 14, pp. 417-27.

18. Hanson, K.J. (1972): Remote Sensing of the Ocean. In: Remote Sensing of the Troposphere (V. Derr, Ed.), U.S. Government Printing Office, Washington, D.C. pp. 22-1 to 22-56.

19. Herman, A. and Jacobson, S.R., (1975). FESTSA: A System for Time Series Analysis, NOAA/AOML, Miami, Fla., Unpublished manuscript.

20. Kattawar, G.W., and Plass, G.N., (1972): Radiative Transfer in the Earth's Atmosphere Ocean System: II Radiance in Atmosphere and Ocean, J. Phys. Ocean. 2, pp. 146-156.

21. Kondrat'ev, K.Y., (Ed), (1973): Radiation Characteristics of the Atmosphere on the Earth's Surface, Amerind. Pub. Co. Pvt. Ltd., New Delhi.

22. Kullenberg, G., (1968): Scattering of Light by Sargasso Sea Water, Deep Sea Res., 15, pp. 423-32. (Note that all the phase functions in the present paper are normalized according to $2\pi \int_0^\pi P(\theta)\sin\theta d\theta = 1$)

23. Maul, G.A., (1975),: An Evaluation of the Use of the Earth Resources Technology Satellite for Observing Ocean Current Boundaries in the Gulf Stream System, NOAA Technical Report ERL 335-AOML 18, Boulder, Colorado, 125 pp.

24. Maul, G.A. (1974): Applications of ERTS Data to Oceanography and the Marine Environment, COSPAR: Approaches to Techniques, Akademie-Verlag, Berlin, pp. 335-347.

25. Maul, G.A. (1973): Infrared Sensing of Ocean Surface Temperature, In: The Second Fifteen Years in Space, A.A.S Vol. 31, pp. 451-64.

26. Maul, G.A., and Gordon, H.R., (1975), On the Use of the Earth Resources Technology Satellite (LANDSAT-1) in Optical Oceanography, Remote Sensing of Environment, 4(2), pp. 95-128.

27. Maul, G.A. and Sidran, M.,(1973): Atmospheric Effects of Ocean Surface Temperature Sensing from the NOAA Satellite Scanning Radiometer, J. Geophys. Res., 78(12), pp. 1909-1916.

28. Maul, G.A. and Sidran, M. (1972): Comment on "Estimation of Sea Surface Temperature from Space" by D. Anding and R. Kauth, Remote Sensing of Environment, 2(3), pp. 165-69.

29. Mueller, J.L., (1973): The Influence of Phytoplankton on Ocean Color Spectra, PhD. Dissertation, Oregon State University, Corvallis, Oregon, 237 pgs.

30. NASA (1975): Report on Active and Planned Spacecraft and Experiments, NS SDC1 WDC-A-R&S, 7501, Goddard Spaceflight Center, Greenbelt, Maryland, pp. 303.

31. Petzold, T.J., Volume Scattering Functions for Selected Waters, Scripps Institution of Oceanography, Univ. of California at San Diego, 1972, SIO Ref. 72-78.

32. Plass, G.N. and Kattawar, G.W., (1972): Effect of Aerosol Variation on Radiance in the Earth's Atmosphere-ocean System, Appl. Opt., 11, pp. 1598-1604.

33. Plass, G.N. and Kattawar, G.W., (1969): Radiative Transfer in an Atmosphere Ocean System, Appl. Opt., 8, pp. 455-66.

34. Preisendorfer, R.W., (1961): Application of Radiative Transfer Theory to Light Measurements in Sea, U.G.G.I., Monogr. 10, pp. 11-30.

35. Richardson, P.L., Strong, A.E., and J.A. Knaus, (1973): Gulf Stream Eddies: Recent Observations in the Western Sargasso Sea, J. Phys. Ocean., 3(3), pp. 297-301.

36. Strickland, J.D.H. and Parsons, R.R. (1968): A Practical Handbook of Seawater Analysis, Fisheries Research Board of Canada, Ottawa, 311 pgs.

37. Tyler, J.E., and Smith, R.C., (1970): Measurements of Spectral Irradiance Underwater, Gordon and Breach, N.Y., 103 pgs.

38. Warnecke, G., Allison, L.J., McMillin, L.M., and K.H. Szekielda, Remote Sensing of Ocean Currents and Sea Surface Temperature Changes Derived from Nimbus II Satellite, J. Phys. Ocean., 1(1), pp. 45-60.

Appendix A

This appendix lists the surface data obtained during the 8-9 January 1974 (GMT) cruises of the R/V VIRGINIA KEY. The geographic positions were determined after the control data were carefully replotted and a best fit of the vessel's location made. Values reported were made using standard oceanographic techniques or modified as explained in section 2.2 of the text.

Cl-a (mg/m^3)	TIME (GMT)	Position
0.15	1957	24° 08.1 N, 81° 34.6 W
0.09	2200	23° 58.8 N, 81° 40.4 W
0.11	2400	23° 47.5 N, 81° 47.2 W

SAMPLES at depth at 1957 GMT at 24° 08.1 N, 81°34.6 W

Depth	Cl-a (mg/m^3)
10 m	0.79
20 m	0.21
30 m	0.25
40 m	0.42
50 m	0.30

SAMPLES at depth at 2200 GMT at 23° 58.8 N, 81° 40.4 W

Depth	Cl-a (mg/m^3)
10 m	0.10
20 m	0.20
30 m	0.35
40 m	0.31
50 m	0.30

TABLE A.2

SALINITY SURFACE SAMPLES

sal(°/oo)	TIME (GMT)	Position
35.996	1314	24° 38.9 N, 81° 08.0 W
35.924	1449	24° 34.5 N, 81° 12.2 W
35.929	1515	24° 30.7 N, 81° 16.3 W
35.921	1719	24° 23.3 N, 81° 21.8 W
36.009	1806	24° 19.1 N, 81° 27.3 W
36.023	1940	24° 10.2 N, 81° 33.7 W
36.017	1958	24° 08.1 N, 81° 34.6 W
36.119	2200	23° 58.8 N, 81° 40.4 W
35.874	2400	23° 47.5 N, 81° 47.2 W
35.918	0110	23° 38.2 N, 81° 52.6 W

Table A.3

Volume Scattering β (45)

Surface Samples

Blue $(m^{-1}sr^{-1} \times 10^{-3})$	Green $(m^{-1}sr^{-1} \times 10^{-3})$	GMT Time	Position
17.3	13.5	1300	24° 40.2 N 81° 07.3 W
13.2	9.9	1314	24° 38.9 N 81° 08.0 W
3.03	3.02	1434	24° 36.5 N 81° 10.6 W
2.61	2.08	1449	24° 34.5 N 81° 12.2 W
2.40	1.60	1504	24° 32.2 N 81° 14.7 W
2.82	2.37	1515	24° 30.7 N 81° 16.3 W
2.69	1.95	1630	24° 27.7 N 81° 16.3 W
3.07	2.15	1645	24° 26.1 N 81° 18.1 W
3.06	2.16	1700	24° 24.6 N 81° 20.2 W
2.16	2.31	1715	24° 23.3 N 81° 21.8 W
3.42	3.09	1750	24° 20.5 N 81° 25.4 W
3.10	2.24	1802	24° 19.1 N 81° 27.3 W
4.02	3.49	1855	24° 16.3 N 81° 31.0 W
2.74	2.49	1910	24° 14.6 N 81° 32.5 W
3.08	1.75	1925	24° 12.4 N 81° 33.5 W
4.54	3.29	1940	24° 10.2 N 81° 33.7 W
5.82	8.44	1957	24° 08.1 N 81° 34.6 W
2.76	2.20	2040	24° 04.5 N 81° 35.6 W
2.73	1.45	2115	24° 03.2 N 81° 37.7 W
3.08	1.98	2130	24° 01.5 N 81° 39.0 W
2.99	1.90	2145	24° 00.5 N 81° 39.8 W
1.65	1.77	2200	23° 58.8 N 81° 40.4 W

1.3

Table A.3 (cont'd)

Volume Scattering β (45)

Blue ($m^{-1}sr^{-1}$ x 10^{-3})	Green ($m^{-1}sr^{-1}$ x 10^{-3})	GMT Time	Position
3.35	2.04	2255	23° 55.8 N 81° 42.0 W
2.63	1.85	2310	23° 53.8 N 81° 43.5 W
2.85	1.83	2325	23° 51.9 N 81° 44.6 W
2.58	1.67	2400	23° 47.5 N 81° 47.2 W
1.92	1.30	0050	23° 40.9 N 81° 51.1 W
1.93	1.28	0110	23° 38.2 N 81° 52.6 W
1.96	1.35	0130	23° 35.7 N 81° 54.1 W
2.19	1.50	0150	23° 33.2 N 81° 55.6 W

Volume Scattering β (45)

Samples at depth at 1314 GMT at 24° 38.9 N, 81° 08.0 W

depth	Blue ($m^{-1}sr^{-1}$ x 10^{-3})	Green ($m^{-1}sr^{-1}$ x 10^{-3})
10 m	2.11	1.83

Samples at depth at 1600 GMT at 24° 29.3 N, 81° 15.5 W

depth	Blue ($m^{-1}sr^{-1}$ x 10^{-3})	Green ($m^{-1}sr^{-1}$ x 10^{-3})
10 m	13.4	11.1
20 m	2.39	1.77
30 m	2.88	2.80
40 m	.2.27	1.86
50 m	1.46	1.42

Table A.3 (cont'd)

Volume Scattering $\beta(45)$

Samples at depth at 1806 GMT at 24° 19.1 N, 81° 27.3 W

depth	Blue ($m^{-1}sr^{-1}$ x 10^{-3})	Green ($m^{-1}sr^{-1}$ x 10^{-3})
10 m	8.07	8.43
20 m	2.57	2.19
30 m	4.37	3.37
40 m	3.34	2.46
50 m	6.87	5.05

Samples at depth at 1957 GMT at 24° 08.1 N, 81° 34.6 W

depth	Blue ($m^{-1}sr^{-1}$ x 10^{-3})	Green ($m^{-1}sr^{-1}$ x 10^{-3})
10 m	5.68	3.78
20 m	4.26	3.66
30 m	4.61	3.73
40 m	3.87	3.26
50 m	4.41	3.55

Samples at depth at 2200 GMT at 23° 58.8 N, 81° 40.4 W

depth	Blue ($m^{-1}sr^{-1}$ x 10^{-3})	Green ($m^{-1}sr^{-1}$ x 10^{-3})
10 m	4.12	2.99
20 m	2.60	1.94
30 m	5.70	4.06
40 m	3.98	3.42
50 m	3.28	2.60

Table A.4
Bucket Temperatures

Temp.(°C)	TIME GMT	Position
24.5	1315	24° 38.9 N, 81° 08.0 W
* 24.8	1434	24° 36.5 N, 81° 10.6 W
* 25.3	1449	24° 34.5 N, 81° 12.2 W
* 25.4	1504	24° 32.2 N, 81° 14.7 W
* 25.0	1630	24° 27.7 N, 81° 16.3 W
25.0	1645	24° 26.1 N, 81° 18.1 W
* 24.5	1700	24° 24.6 N, 81° 20.2 W
* 24.3	1750	24° 20.5 N, 81° 25.4 W
* 24.4	1805	24° 19.1 N, 81° 27.3 W
* 24.5	1855	24° 16.3 N, 81° 31.0 W
* 24.5	1910	24° 14.6 N, 81° 32.5 W
* 24.7	1925	24° 12.4 N, 81° 33.5 W
* 24.4	1940	24° 10.2 N, 81° 33.7 W
24.4	2010	24° 07.0 N, 81° 34.6 W
* 24.6	2040	24° 04.5 N, 81° 35.6 W
* 24.9	2115	24° 03.2 N, 81° 37.7 W
* 24.9	2130	24° 01.5 N, 81° 39.0 W
* 24.8	2145	24° 00.5 N, 81° 39.8 W
25.0	2200	23° 58.8 N, 81° 40.4 W
* 25.0	2255	23° 55.8 N, 81° 42.0 W
* 25.1	2310	23° 53.8 N, 81° 43.5 W
* 25.5	2325	23° 51.9 N, 81° 44.6 W
* 25.5	2340	23° 49.9 N, 81° 45.8 W
25.5	2400	23° 47.5 N, 81° 47.2 W

66

Table A.4 (cont.)
Bucket Temperatures

Temp. (°C)	TIME GMT	Position
* 26.1	0050	23° 40.9 N, 81° 51.1 W
* 26.1	0110	23° 38.2 N, 81° 52.6 W
* 26.2	0130	23° 35.7 N, 81° 54.1 W
* 26.3	0150	23° 33.2 N, 81° 55.6 W

* Denotes XBT casts.

67

APPENDIX B.

Pressure (mb)	Temp.(^{O}C)	R.H. (%)	
			Surface
1021	024.8	79	
1011	023.5	82	Dry Bulb: 24.º9C
1000	023.0	85	Wet Bulb: 22.º2C
902	017.1	86	RH: 79%
869	015.9	63	Wind Dir: 050°T
850	015.1	64	Wind Spd: 5 mps
808	012.8	66	Clouds 1/10 cu
799	012.2	34	ϕ 24°35'N
788	011.2	72	λ 81°42'W
744	009.9	66	
740	008.3	72	
722	008.5	30	
700	007.8	31	
671	005.2	55	
640	003.3	42	
621	003.1	22	
530	-06.3	21	
500	-09.4	13	
470	-12.4	10	
384	-24.9	14	
300	-39.1	14	
250	-48.9		
224	-50.3		
212	-48.9		
200	-50.3		
150	-62.6		
100	-77.1		
070	-75.7		
066	-75.2		
061	-71.5		
058	-72.7		
054	-67.6		
050	-67.8		
045	-64.7		
043	-58.1		
030	-51.2		
023	-46.3		
020	-47.4		
017	-48.0		
016	-48.2		
13.5	-43.9		

APPENDIX C

This appendix lists the Monte Carlo simulations of radiances I_1 and I_2 as described in Section 4.2.2. Wavelengths at which the OxN and lxN atmospheric aerosol concentrations were computed for all 400, 500, 600, and 780 nm. The cosine of ten zenith angles (μ) were the independent variables. I_1 and I_2 are normalized to unit solar flux on a surface normal to the solar beam.

Wavelength = 400 nm   Aerosol = OxN

μ	$I_1(\mu)$	$I_2(\mu)$
.00		
	.10089+00	.53255-01
.10		
	.88850-01	.72697-01
.20		
	.78011-01	.87278-01
.30		
	.67433-01	.98883-01
.40		
	.57839-01	.10661+00
.50		
	.52975-01	.11159+00
.60		
	.48109-01	.11406+00
.70		
	.46607-01	.11634+00
.80		
	.44244-01	.11615+00
.90		
	.42872-01	.11701+00
.95		
	.75049-01	.11782+00
1.00		

70

Wavelength = 400 nm   Aerosol = 1xN

μ	$I_1(\mu)$	$I_2(\mu)$
.00		
	.93753-01	.51310-01
.10		
	.90653-01	.63140-01
.20		
	.83232-01	.77826-01
.30		
	.76449-01	.87640-01
.40		
	.67122-01	.96479-01
..50		
	.61046-01	.10118+00
.60		
	.57118-01	.10457+00
.70		
	.54662-01	.10757+00
.80		
	.52434-01	.10919+00
.90		
	.52278-01	.10916+00
.95		
	.71513-01	.10906+00
1.00		

71

Wavelength = 500 nm   Aerosol = 0xN

μ	$I_1(\mu)$	$I_2(\mu)$
.00		
	.63253-01	.59700-01
.10		
	.52971-01	.91621-01
.20		
	.37429-01	.10902+00
.30		
	.29710-01	.12474+00
.40		
	.24246-01	.13138+00
.50		
	.22112-01	.13641+00
.60		
	.19925-01	.13898+00
.70		
	.19015-01	.14171+00
.80		
	.18002-01	.14225+00
.90		
	.17044-01	.14326+00
.95		
	.67308-01	.14203+00
1.00		

Wavelength = 500 nm   Aerosol = 1xN

     μ $I_1(\mu)$ $I_2(\mu)$

.00

              .62318-01   .56038-01
.10

              .59056-01   .75227-01
.20

              .49220-01   .96058-01
.30

              .41716-01   .11022+00
.40

              .35218-01   .11781+00
.50

              .31928-01   .12576+00
.60

              .27678-01   .12875+00
.70

              .26638-01   .13063+00
.80

              .25573-01   .13228+00
.90

              .26419-01   .13315+00
.95

              .57385-01   .13155+00
1.00

73

Wavelength = 600 ṅm

Aerosol = 0xN

μ	$I_1(\mu)$	$I_2(\mu)$
.00	.30110-01	.42002-01
.10	.24508-01	.80947-01
.20	.17292-01	.10497+00
.30	.13224-01	.12254+00
.40	.10725-01	.13037+00
.50	.98865-02	.13672+00
.60	.90777-02	.14052+00
.70	.88360-02	.14304+00
.80	.80934-02	.14358+00
.90	.77006-02	.14664+00
.95	.61865-01	.14694+00
1.00		

Wavelength = 600 nm   Aerosol = 1xN

μ	$I_1(\mu)$	$I_2(\mu)$
.00		
	.27632-01	.36991-01
.10		
	.36531-01	.67189-01
.20		
	.29628-01	.92357-01
.30		
	.25526-01	.10823+00
.40		
	.21423-01	.11883+00
.50		
	.17841-01	.12614+00
.60		
	.16190-01	.13059+00
.70		
	.15107-01	.13303+00
.80		
	.14509-01	.13448+00
.90		
	.16199-01	.13524+00
.95		
	.52310-01	.13560+00
1.00		

Wavelength = 780 nm   Aerosol = 0xN

μ	$I_1(\mu)$	$I_2(\mu)$
.00		
	.27838-01	.69923-01
.10		
	.13026-01	.10854+00
.20		
	.76052-02	.13086+00
.30		
	.51505-02	.14849+00
.40		
	.42167-02	.15502+00
.50		
	.37095-02	.16096+00
.60		
	.34865-02	.16342+00
.70		
	.33889-02	.16269+00
.80		
	.30901-02	.16464+00
.90		
	.30811-02	.16649+00
.95		
	.65909-01	.16607+00
1.00		

Wavelength = 780 nm   Aerosol = 1xN

μ	$I_1(\mu)$	$I_2(\mu)$
.00		
	.40506-01	.67910-01
.10		
	.33748-01	.95346-01
.20		
	.24905-01	.11832+00
.30		
	.18224-01	.13459+00
.40		
	.14512-01	.14180+00
.50		
	.11931-01	.14856+00
.60		
	.10491-01	.15236+00
.70		
	.98166-02	.15399+00
.80		
	.98476-02	.15395+00
.90		
	.11295-01	.15613+00
.95		
	.57149-01	.15511+00
1.00		